Dissertation

Study of SiPM-based Photon-counting Computed Tomography and Image Reconstruction Algorithms for Low Radiation Dose

Division of Mathematical and Physical Sciences
Graduate school of Natural Science & Technology
Kanazawa University

Student ID No. 2124012003
Name Daichi Sato
Chief advisor Makoto Arimoto
Date of Submission February 25, 2024

Abstract

X-ray computed tomography (CT) is an important non-destructive visualization technology for three-dimensional structures inside the human body. For lesions that are difficult to be identified using CT imaging alone, medical CT imaging using a contrast agent (i.e., contrast-enhanced CT scanning) is performed to obtain CT images that highlight the lesions for more accurate diagnoses. However, in conventional X-ray CT systems, it is difficult to read individual X-ray signals because the detector consists of a photodiode and a gadolinium oxysulfide scintillator. The time scale of the X-ray photon signal ranges from microseconds to milliseconds, which are integrated and read out in the current form. This results in the loss of energy information of the incident X-rays, making it difficult to identify the target material and quantitatively evaluate physical parameters such as the concentration. To overcome these limitations, photon-counting (PC) CT has attracted considerable attention as a novel technique.

PC-CT can detect individual X-ray photons in pulse form and utilize their energy information to visualize only the target material. Therefore, if PC-CT is used as a contrast-enhanced CT, the position and concentration of the contrast agent injected into the body can be discriminated and visualized with greater precision, and it is expected to detect small lesions that might have been overlooked in the past. On the other hand, one of the problems with contrast-enhanced CT is that as the contrast agent travels around the body, the position and concentration of the contrast agent become highly indefinite. This cannot be avoided even when photon-counting CT is used. Therefore, it is important to complete CT imaging in as short a time as possible. In addition, from the viewpoint of patient exposure, it is desirable to perform imaging in a short time. Therefore, to realize short-time and low-dose imaging, we focused on imaging methods called sparse-view CT. Sparse-view CT is a technique that reconstructs images with fewer projections than the number of projection data based on the sampling theorem. Since the number of projections is proportional to the imaging time and radiation dose considering ideal conditions, the fewer the number of projections, the shorter the time and lower the radiation dose. Since this methods require the application of a dedicated image reconstruction algorithm to the projection data, it is more convenient from the viewpoint of image quality evaluation to obtain projection data by actually taking images while changing conditions in detail, rather than processing CT images from a publicly available database. In addition, there is only one type of PC-CT currently in clinical application, and it was just marketed in 2023, so there are few samples of PC-CT images in the publicly available database. In view of the above, we decided to actually construct a PC-CT system and apply a compressed sensing-based image reconstruction algorithm to the obtained measurement data and we demonstrate the feasibility of contrast-enhanced CT using PC-CT.

In this study, we validated the performance of sparse-view CT by combining a silicon photomultiplier (SiPM) based PC-CT, which is relatively inexpensive to construct, and a compressed sensing (CS)-based image reconstruction algorithm. In the sparse-view CT, sparse-view sampled projection data was created by acquiring the projection data to satisfy the sampling theorem and then downsampling the projection. A CS-based image reconstruction algorithm was then applied to each projection data, and the image quality of the resulting sparse-view CT images was evaluated.

Consequently, sparse-view CT images were successfully reconstructed, and the image quality was maintained even after downsampling the projection data (downsampling ratios of 1/10 and 1/2 for the rod phantom and mouse model, respectively). Thus, the imaging time and radiation dose could be remarkably reduced (by a factor of 10 or 2) in the sparse-view CT indicating that contrast-enhanced CT with quantitative evaluation is feasible by combining CS-based image reconstruction algorithms with PC-CT.

Contents

List of Figures

List of Tables

Chapter 1

X-ray Computed Tomography

X-ray computed tomography (X-ray CT) is an instrument for imaging the cross-sectional structure of an object, utilizing the property of X-rays to attenuate in intensity as they pass through the object. Because it can observe the internal structure of an object without destroying it, it is used in a variety of fields, such as to investigate the deterioration of industrial products and to analyze the composition of valuable rock samples. It is particularly popular in the medical field, where it is widely used for diagnosis and follow-up observation of lesions. Here, we will introduce the advantages and disadvantages of X-ray CT by looking at how it has contributed to medicine and the relationship between the two, and propose a new CT system for diagnostic medicine.

1.1 Historical background

The X-ray CT was invented and developed virtually independently by G. N. Hounsfield, an engineer at EMI in England, and reported in 1973 [1–3]. While conventional radiography (so-called roentgenography) images the human body as a two-dimensional transmission image, X-ray CT provides a cross-sectional image of the inside of the body. In particular, it was difficult to visualize the structures inside the cranium, which are composed of bones with high attenuation coefficients, using radiography (FIg. 1.1). The advent of CT revolutionized the medical world at the time by enabling nondestructive visualization of these structures. On the other hand, CT images were not sufficient in terms of shading, spatial resolution, and temporal resolution, and these have been improved up to the present day. For example, scanning time has been reduced from about 4 minutes per rotation in the early 1970s to about 0.3 seconds, and image reconstruction time has been reduced from several hours to milliseconds, which together with the development of the latest CT technology has dramatically improved examination throughput (Fig. 1.2). In addition, spatial resolution has been improved from 3 mm to 0.14 mm [4], contrast-enhanced CT examinations using contrast agents with high X-ray attenuation have been put to practical use, and image reconstruction methods with high image quality have been proposed even with low doses of radiation. Even today, however, there are many technical challenges. In the following, contrast-enhanced CT examinations and low-dose CT will be discussed in depth.

1.2 Technical challenges

1.2.1 Contrast-enhanced CT

In current clinical practice, contrast-enhanced CT scans are performed using iodine-based contrast agents (e.g., iopamilon) [5–7]. Iodine absorbs more X-rays than other tissues in the body (water, adipose, etc.), so when iodine is administered into the body, the pixel value of the CT image is higher in areas where iodine is present. This property is used, for example, to visualize tumors. Since tumors generally have high blood flow, the amount of iodine flowing in the blood vessels is relatively high. As a result, the area where the tumor is located is emphasized and used to

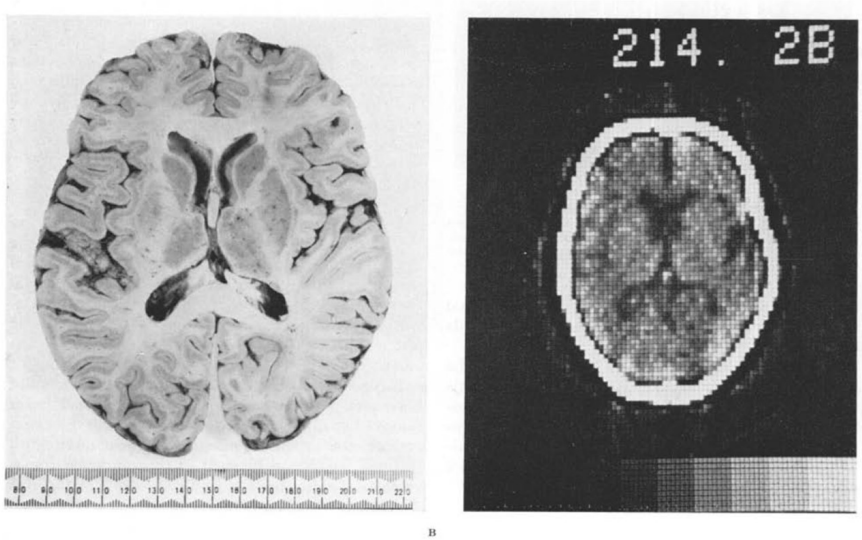

Figure 1.1: CT image of the head at the dawn of CT development. The structure of the brain inside the cranium can be seen. A portion of Figure 5 in the citation [2] is excerpted.

Figure 1.2: Ultra-high resolution CT. (Aquilion Precision, Canon Medical Systems, `https://jp.medical.canon/products/computed-tomography/aq_precision`)

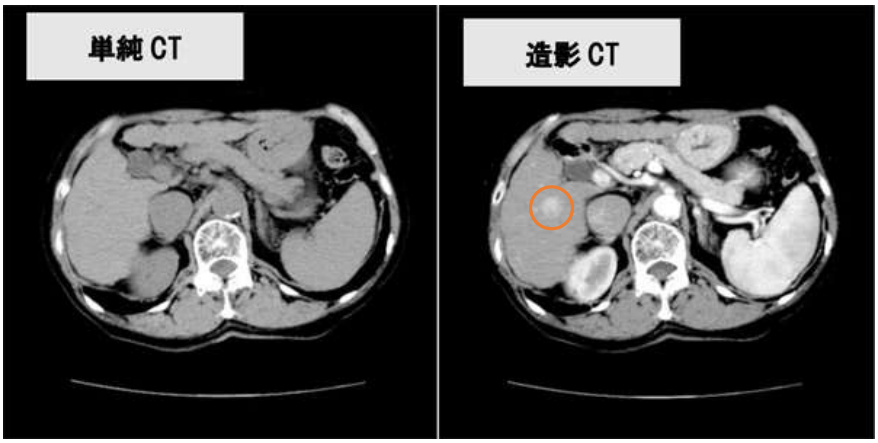

Figure 1.3: Left: Simple CT image of the abdomen. Right: Contrast-enhanced CT image with iodine contrast agnet. The iodine contrast enhancement can be seen in the area surrounded by the orange circle. (`https://midori-hp.or.jp/radiology-blog/web20230807/`)

Table 1.1: Number of CT examinations in 2014 [9].

Rank	Country and Region	CT exams per 1,000 ppopulation
1st	United States	255
2nd	Japan	231
3rd	Luxembourg	207
4th	Belgium	193
5th	Iceland	180
Average	OECD	133

determine the diagnosis. Fig. 1.3 left shows a simple CT image of the abdomen without iodine contrast agnet and right shows a contrast-enhaced CT image of the abdomen with the contrast agent administration. In the simple CT image, the liver appears to be a homogeneous tissue, but with the iodine contrast agent administration, certain areas of the liver are seen to be enhanced by the iodine. The diagnostician suspects the presence of a tumor in the liver and performs pathology or other tests to definitively diagnose whether the tumor is malignant (i.e., cancerous) or not. The problem is that small tumors can be missed by the diagnostician; if they are missed at the CT image reading stage, the next diagnostic step, such as pathology, will not be performed. It is said that it takes 1–2 years for a malignant tumor to grow from 1 cm to 2 cm, so if regular checkups are not performed, detection will be delayed and can have serious effects on the body. Treatment of advanced cancers such as stage-IV is difficult in some cases and may be limited to palliative care. Therefore, early detection of small cancer is important in terms of extending healthy life expectancy. In particular, a new system to evaluate malignancy is required so that tumors smaller than 1 cm can be detected without relying on the doctor's eye.

1.2.2 Low-dose CT

In Japan, it has been pointed out that the total exposure dose has increased with the increase in CT imaging opportunities, and a reduction in irradiation dose is desired (Table 1.1, 1.2). In fact, medical exposure accounts for about 65% of the annual radiation dose, and among medical exposures, exposure from CTs accounts for nearly 50% [8]. It is most effective to reduce medical exposure from CT imaging.

Table 1.2: Number of CT installations in 2014 [9].

Rank	Country and Region	CT scanners per millon ppopulation
1st	Japan	107
2nd	Australia	56
3rd	United States	41
4th	Iceland	40
5th	Denmark	38
Average	OECD	27

1.3 Overcoming techniques

As we have seen in the previous sections, conventional CT systems have two issues to overcome: the detection of small lesions whose shading is not visible even with contrast agents, and the achievement of equal or better image quality with a lower exposure dose. A system that can achieve these goals is the next-generation CT system using a photon-counting detector, which has been the focus of much attention in recent years. In addition, there is an imaging method called sparse-view image reconstruction, which is designed to achieve lower radiation dose.

1.3.1 Photon-counting CT

Conventional X-ray CT is widely utilized in the medical field due to its ability to non-destructively observe the three-dimensional internal structure of the human body. However, the current setup, which includes a detector composed of a photodiode and a gadolinium oxy sulfide (GOS) scintillator, integrates and reads out the X-ray signal as a current signal [10, 11]. This is because the time constant of the X-ray signal is long, making it difficult to read each X-ray signal individually; the singanl height of the X-ray is proportional to its X-ray energy, resulting in the loss of energy information in the X-ray signal and weakening its ability to identify the target material. (Top right of Fig. 1.4). This further hinders the quantitative evaluation of the spatial and temporal distribution of contrast agent concentration in contrast-enhanced CT examinations. In recent years, photon-counting (PC) CT has attracted much attention and is widely used as an approach to solve these problems [12–35].

PC-CT operates by detecting individual X-ray photons in the form of pulses. The height of the pulse signal is directly proportional to its energy, enabling the setting of multiple energy thresholds to capture information on the number and energy of X-rays within each interval. This relationship between X-ray interactions and materials enables the visualization of specific target materials within a subject. Systems under development worldwide are direct conversion PC-CTs based on CdTe or CdZnTe sensors, and those currently being introduced into clinical practice are also direct-conversion (e.g., NAEOTOM Alpha, Siemens Healthineers) [36–42]. However, the cost of this system is significantly higher than that of conventional systems, which may limit its adoption. To address this, we have developed an indirect conversion system based on silicon photomultiplier (SiPM) technology, which combines a multi-pixel photon counter (MPPC) and a cerium-doped yttrium-gadolinium-aluminum-gallium garnet (YGAG:Ce) scintillator with a short decay time constant, providing a cost-effective alternative to direct conversion PC-CT [43–45]. Indirect conversion detectors using scintillators have a larger detection area than direct conversion systems using CdZnTe, and the thicker scintillators provide higher detection efficiency for X-rays.

We have previously reported CT imaging results of static phantoms containing iodine-based contrast agents using our SiPM-based PC-CT systems [44–46]. However, for future clinical applications, it is crucial to demonstrate the in vivo CT imaging capability using live subjects. Therefore, we verified the in-vivo CT imaging capability of the PC-CT system by injecting iodine contrast agent intravenously through the tail into a mouse model put to sleep by anesthesia and visualizing the concentration of iodine distributed in the body [47].

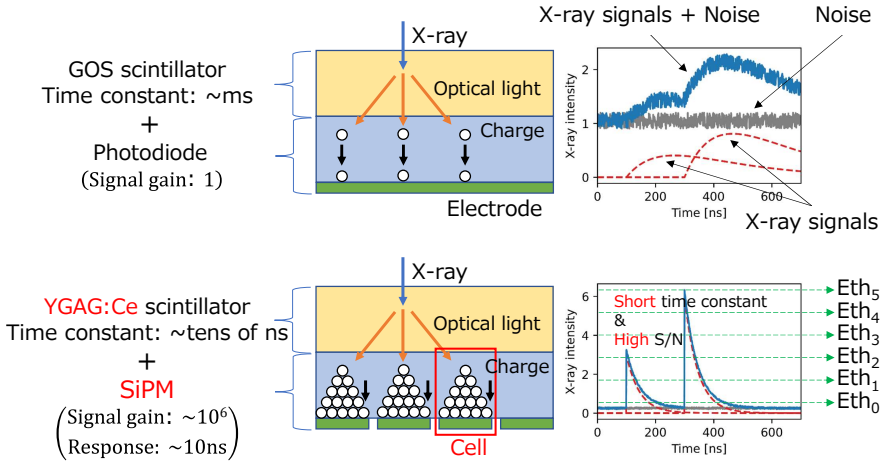

Figure 1.4: Top and Bottom: Concepts of conventional CT and indirect-conversion PC-CT system. Left: X-ray detector configuration. The conventional model combines a GOS scintillator and a photodiode. The indirect conversion PC-CT we are aiming for is realized by combining a YGAG:Ce scintillator with a short time constant and a SiPM (MPPC) with an internal signal amplification mechanism. Right: Predicted X-ray signal waveform. Compared to the conventional type, the PC-CT system achieves shorter decay time and higher signal-to-noise ratio (S/N).

1.3.2 Sparse-view CT

Sparse-view reconstruction in X-ray CT offers the advantage of reduced radiation dosage and faster imaging by requiring minimal measured data for image reconstruction [48–72]. Fig. 1.5 shows the concept of general CT imaging and sparse-view CT imaging. In conventional CT, the transmitted intensity of X-rays emitted from an X-ray tube is measured by an X-ray detector. This measurement is performed at various angles in the same plane to satisfy the sampling theorem, and usually about 1000–2000 measurement data are obtained. Sparse-view CT, on the other hand, is an attempt to perform imaging with a number of measurement data that is much less than the sampling theorem (about 10–100 measurements). However, it is known that the application of the filtered back-projection (FBP), a classical image-reconstruction method, to these sparse measurement data causes streak artifacts in the resulting CT images, which has been a longstanding problem (Top and Center of Fig. 1.6). In the 2000s, an innovative technique called compressed sensing (CS) theory was reported [73,74], which led to a major advance in sparse-view CT [75–86]. The CS-based image reconstruction algorithm is a method that attempts to obtain a true CT image by updating the reconstructed image in a sequential and approximate manner. It has been about 20 years since the first CS-based image reconstruction algorithm was proposed for CT image generation, and it is still expanding due to various studies. For example, numerical image analysis has been performed by simulation to investigate more accurate image reconstruction methods, and the results have been applied to real data from dual-energy CTs equipped with energy-integrating detectors, which are the main equipment used in clinical practice [87]. In addition, machine learning-based sparse-view CT is also proposed, indicating that the field is developing more and more, incorporating recent trends [88]. Despite the growing literature on machine learning-based sparse-view CT, CS-based sparse-view CT using PC-CT is almost non-existent [89]. This is because PC-CT is still a research-phase system and few clinical devices have been implemented. Looking ahead to the future of clinical practice, it is clear that PC-CT is a suitable system for the next generation, and it should be well worthwhile to examine the applicability of PC-CT in advance of such a system. In addition, there is no case in which sparse-view reconstruction has been applied to contrast agent concentration estimation maps. Through the performance evaluation of this system, we aim to realize even lower exposure dose and shorter imaging time for contrast-enhanced CT examinations, thereby providing more reliable medical diagnosis for patients. Therefore, we integrated a CS-based image-reconstruction algorithm with an SiPM-based PC-CT system developed in our previous

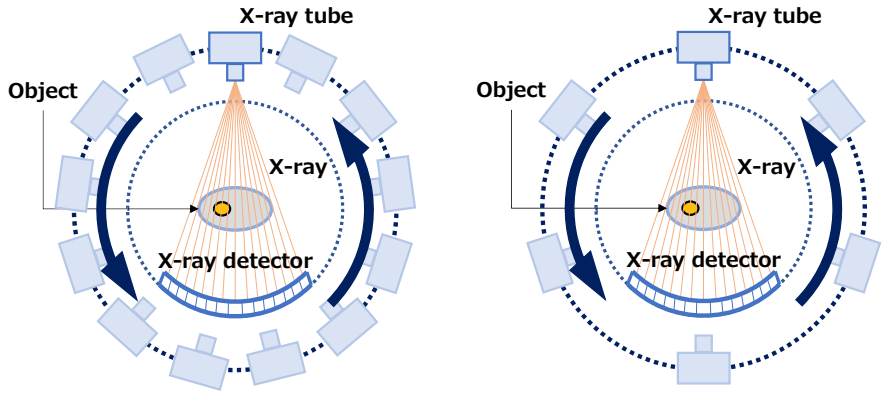

Figure 1.5: image reconstruction Left: Conventional CT imaging. Generally, about 1000-2000 imaging (projection) data are acquired, and CT images are obtained by image reconstruction. Right: Sparse-view CT imaging. CT imaging is performed with projection data reduced to 1/10 1/100 of that of conventional CT imaging. The image reconstruction method, which does not generate image noise (artifacts) even with less projection data, realizes short-time and low-dose CT imaging.

work [43–45].

In this research, we present the preliminary findings of a comprehensive evaluation of sparse-view CT images acquired using our PC-CT system [90]. We utilized static phantoms mimicking an iodine-containing contrast agent and a mouse model injected with such contrast agent, previously employed for image analysis with FBP [46, 47, 91]. Since iodine contrast agents are the most widely used in clinical practice today, validation of the performance of CT imaging with this as a subject could serve as a basis for contrast CT examinations using PC-CT. Subsequently, CT scanning was conducted, followed by the application of a CS-based image-reconstruction algorithm incorporating total-variation (TV) minimization to sparsely sampled projection data across various downsampling ratios. TV minimization is the most fundamental method in CS-based image reconstruction algorithms. We evaluated the image quality of the resulting CT images to ascertain the optimal downsampling ratios while preserving image quality, extending the assessment to iodine concentration maps. The outcomes highlight the effectiveness of the CS-based image-reconstruction algorithm in PC-CT, showcasing its significant potential for reducing radiation exposure and imaging duration.

1.4 Aim of this paper

In this paper, we constructed a PC-CT system using our originally developed phovton-counting detector and evaluated its performance for contrast CT imaging using iodine contrast agents (Chapter 3). This shows that a SiPM-based PC-CT system can also estimate the concentration of contrast agents, and we propose this system as a basic system for clinical application. In addition, sparse-view CT imaging was performed using the projection data obtained by the constructed system to evaluate the image quality (Chapter 4). The effect of image quality on real photon counting CT images will be verified and the possibility of reducing the dose will be discussed.

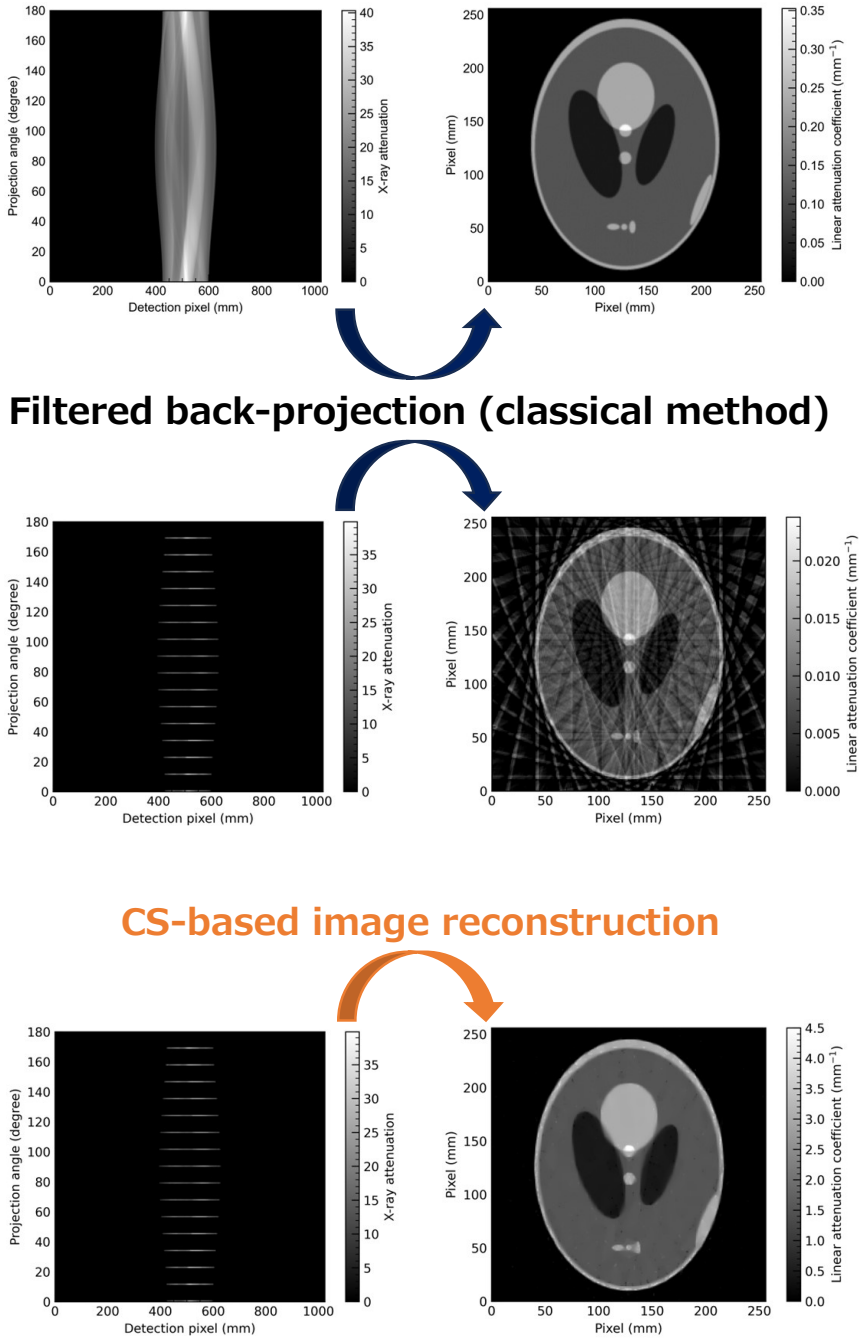

Figure 1.6: Simulation results of CT images from various image reconstruction methods. Left: Measured (projected) data. Right: reconstructed CT images. Top: case where the classical image reconstruction method (FBP) is used on the measured data satisfying the sampling theorem. Center: extreme failure of the sampling theorem; image reconstruction using FBP results in artifacts on the reconstructed CT image. Bottom: using a compressed sensing-based image reconstruction algorithm, which reduces artifacts on the CT image.

Chapter 2

Principle of X-ray CT

The purpose of an X-ray CT system is to measure the distribution of how much X-rays are attenuated (i.e., the linear attenuation coefficient) at various sites inside the body. The linear attenuation coefficient has different values depending on the elements constituting the material and the energy of the irradiated X-rays. Therefore, knowing the distribution of the linear attenuation coefficient is useful for estimating the structure of the inside of the body and the elements that make up the body, and can be a clue to the diagnosis of lesions. In clinical practice, a tomographic image of a subject (i.e., the CT image) is produced by creating a two-dimensional distribution of CT values from the acquired two-dimensional distribution of line attenuation coefficients. This section introduces the principles and theories necessary for the process of obtaining the CT images.

2.1 X-ray

X-rays are electromagnetic waves with a specific wavelength range, discovered by W.C. Roentgen in 1895. Its generation mechanism originates from the transition of orbital electrons and kinetic energy of free electrons. We will look at its characteristics below.

2.1.1 Spectrum

X-rays are classified into bremsstrahlung X-rays (continuous X-rays) and characteristic X-rays. Bremsstrahlung X-rays are produced when a charged particle incident on a material loses energy in the Coulomb field of its nucleus. The energy of the generated bremsstrahlung X-ray is equal to the energy lost by the charged particle. Since the distance over which the charged particles pass near the nucleus of the target material varies, the energy deprived also varies depending on the distance. Therefore, bremsstrahlung X-ray exhibits a continuous energy spectrum produced by X-rays with various energies. Characteristic X-rays, on the other hand, are produced when the outer-shell orbital electrons of an atom transition to the inner-shell due to ionization effects caused by radiation. It shows a single energy spectrum corresponding to the difference in binding energy of the orbital electrons of the target material.

Here, Figure 2.1 shows multiple X-ray spectra generated when electrons accelerated by an X-ray tube with tube voltages set at 80, 100, and 120 kV collide with a tungsten target. This is a simulation using SpekPy [92]. The conditions are as follows. Target material: tungsten, anode angle: 12 degrees, filter: Al with a thickness of 1.0 mm. X-rays with continuous energy due to bremsstrahlung and K-shell characteristic X-rays of tungsten can be seen in Figure 2.1. Diagnostic X-ray generators are often used with a tube voltage of 80-140 kV.

2.1.2 Interaction of photons in materials

All radiation interacts directly with the atoms that make up matter. In other words, a single radiation interacts with a single atom, regardless of the structure of the compound or other material

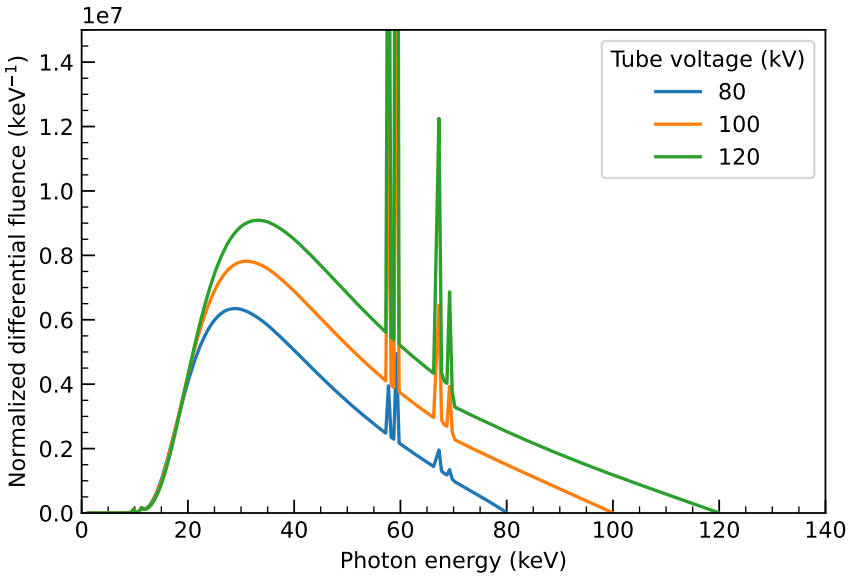

Figure 2.1: X-ray spectra for various tube voltages. The specific peaks indicate characteristic X-rays of tungsten, and the other smooth curves are continuous X-ray spectra due to bremsstrahlung. The tube voltages of the X-ray tube corresponds to the maximum energy of continuous X-rays. In addition, the intensity on the low energy side (lower than 30 keV) is suppressed because of the transmission through a 1.5 mm thick aluminum filter.

of which the atom is a part. We will discuss two of these interactions that are closely related to X-ray CT: the photoelectric effect and Compton scattering.

The photoelectric effect is a phenomenon in which the energy of a photon incident on a material is imparted to the orbital electrons of all atoms, ionizing them. The photoelectric effect begins to occur when the binding energy of the orbital electrons is exceeded. The orbital electrons emitted by the ionization are called photoelectrons. Since the incident photons are completely annihilated, the photoelectric effect is also called photoelectric absorption. For the photoelectric effect to occur, the incident photon must have an energy greater than the ionization energy. Here, the energy of the incident photon is $h\nu$ and the ionization energy of the orbital electron is I, the energy E received by the emitted photoelectron is expressed as:

$$E = h\nu - I. \tag{2.1}$$

The probability of the photoelectric effect occurring increases rapidly with increasing atomic number and decreases rapidly with increasing photon energy; the reaction cross section σ_{photo} of photoelectric absorption per atomic number is approximated as follows

$$\sigma_f \propto \frac{Z^n}{E^{3.5}}, \tag{2.2}$$

where Z is a atomic number, n has a value of 4–5. In the diagnostic X-ray energy range of 100 keV, the photoelectric effect is an important interaction and plays an important role in the formation of diagnostic X-ray images, especially those that display differences in atomic number, i.e., material differences (e.g., bone vs. soft tissue).

Compton scattering is a phenomenon in which part of the energy of an incident photon is given to an orbital electron, which is emitted as a recoil electron upon ionization, and the scattered photon is ejected with the remaining energy. Compton scattering is more likely to occur when the energy of the incident photon is higher than the binding energy of the orbital electrons, especially when the energy is tens of keV to several MeV. In other words, Compton scattering can be said to be an interaction between a photon and a free electron, since the binding energy of the orbital

electrons is negligible. The energy $h\nu'$ of the emitted scattered photon can be described by the momentum and energy conservation laws as follows:

$$h\nu' = \frac{h\nu}{1 + \dfrac{h\nu}{m_0c^2}(1 - \cos\theta)}, \tag{2.3}$$

where m_0 is the electron mass and θ is the scattering angle. Since the energy of recoil electrons Er is simply the energy of incident photons minus the energy of scattered photons, it can be calculated as follows.

$$E_r = h\nu - h\nu' = h\nu \left\{ 1 - \frac{1}{1 + \dfrac{h\nu}{m_0c^2}(1 - \cos\theta)} \right\}. \tag{2.4}$$

Here, when the energy of the incident photon is much smaller than the rest energy of the electron ($h\nu \ll m_0c^2 = 0.51\,\mathrm{MeV}$), from Eq. 2.3 and 2.4, the energy of the scattered photon is $h\nu' \approx h\nu$ and the energy of the recoil electron is $E_r \approx 0$. This is nothing but Thomson scattering. In contrast, in the region where the incident photon energy is much larger than the rest energy ($h\nu \gg m_0c^2$), the scattered photon energy can be expressed as $h\nu' \approx m_0c^2/(1 - \cos\theta)$. Eq. 2.3 also shows that $h\nu'$ has a maximum at $\cos\theta = 0.$ and a minimum at $\cos\theta = 180.$ Thus, since the energy of scattered photons varies with the scattering angle, the energy of scattered photons exhibits a continuous spectrum when a large number of photons are incident. The probability of Compton scattering and the angular distribution of scattered photons can be expressed in terms of the differential scattering cross section for a small solid angle $d\Omega$ in the angle θ direction, which is shown from the Klein-Nishina formula as follows.

$$\frac{d\sigma_e}{d\Omega} = \frac{r_0^2}{2}(1 + \cos^2\theta) \cdot \left(\frac{1}{1 + \alpha(1 - \cos\theta)} \right)^2 \cdot \left(1 + \frac{\alpha^2(1 - \cos\theta)^2}{(1 + \cos^2\theta)(1 + \alpha(1 - \cos\theta))} \right). \tag{2.5}$$

where $\sigma = h\nu/m_0c^2$ and r_0 is the classical electron radius. σ_e is the Compton scattering cross section per electron, so the reaction cross section σ_c for Compton scattering per atom in a material with atomic number Z is expressed as follows:

$$\sigma_c \propto \frac{Z}{E}. \tag{2.6}$$

The reaction cross section for electron-pair production is $\sigma_p \propto Z^2$. Therefore, the relationship between atomic number (reaction cross section) and photon energy is as shown in Figure 2.2. From Figure 2.2, it can be seen that the photoelectric effect is dominant at energies of 100 keV, which is the energy of X-rays typically used in diagnostic X-ray systems.

2.2 X-ray detector

In Section 2.1.2, we discussed the interaction between X-rays and matter. In this section, we describe the methods of detecting X-rays using the aforementioned interaction, especially the features and principles of semiconductor and scintillation detectors.

2.2.1 Semiconductor detectors

Semiconductor detectors convert incident high-energy charged particles into electron-hole pairs, which are further converted into electrical signals such as charge and voltage so that their intensity and energy can be extracted. One of the features of semiconductor detectors is their excellent energy resolution. The following is a more detailed description of the charged particle detection process.

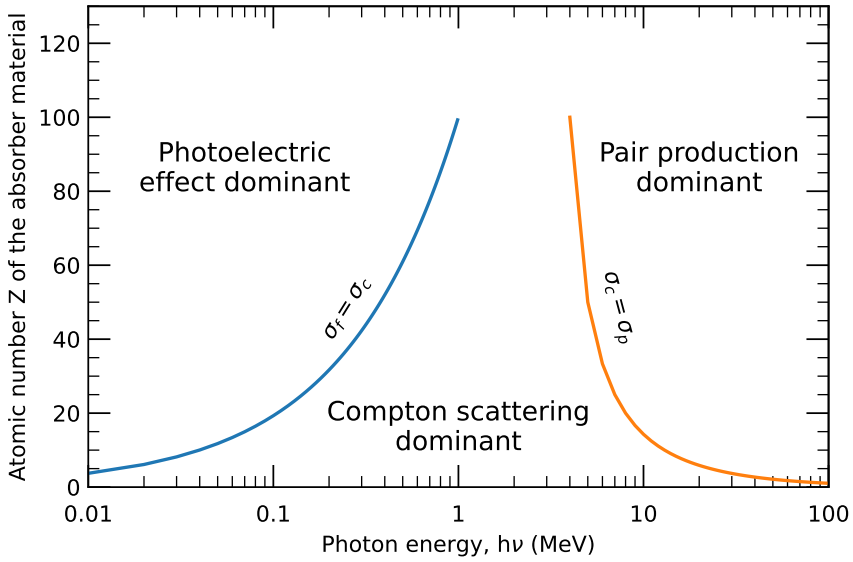

Figure 2.2: The blue curve shows the case where the reaction cross section σ_f of the photoelectric effect and the reaction cross section σ_c of Compton scattering coincide. The orange curve shows the case where the reaction cross sections of Compton scattering and pair production are equal.

1. When radiation strikes a semiconductor, electrons transition from the valence band to the conduction band along their trajectory, producing electron-hole pairs. The number of electron-hole pairs produced, N0, is proportional to the energy of the incident charged particle and can be calculated as follows:

$$N_0 = \frac{E_0}{\epsilon}, \tag{2.7}$$

where ϵ is the average energy required to produce a single electron-hole pair, and has different values for different semiconductor materials.

2. The electrons and holes generated along the particle trajectory spread by diffusion, but the electrons move to the n-side electrode and holes move to the p-side electrode along the electric field E generated by the applied reverse bias. The velocity of electrons (v_e) and holes (v_h) at this time can be calculated from Eq. 2.9. where μ_e and μ_h are the mobility of electrons and holes, respectively.

$$v_e\,[\mathrm{cm\,s^{-1}}] = \mu_e\,[\mathrm{cm^2\,V^{-1}\,s^{-1}}] \cdot E\,[\mathrm{cm^{-1}\,V}] \tag{2.8}$$

$$v_h\,[\mathrm{cm\,s^{-1}}] = \mu_h\,[\mathrm{cm^2\,V^{-1}\,s^{-1}}] \cdot E\,[\mathrm{cm^{-1}\,V}] \tag{2.9}$$

3. Finally, an electrical signal equivalent to the charge Q of the aggregated N electron-hole pairs ($Q[C] = 1.602 \times 10^{19} \cdot N$) is output.

The above is the detection principle of semiconductor detection, which is basically the same as the principle of other detectors such as gas detectors, only the substance is changed. However, semiconductor detectors have a smaller ϵ than other detectors. As a result, a large number of electron-hole pairs can be generated for a single incident charged particle, and this allows them to have excellent energy resolution. Table 2.1 lists the physical properties of semiconductors (Si, Ge, and CdTe), which are currently mainly used in detectors.

In clinical practice, compound semiconductors such as CdTe are generally used. Si and Ge are superior in terms of energy resolution because they can produce a large number of electron-hole pairs at a time, but Si has a small atomic number and is hardly sensitive to X-rays above 100 keV. Ge has a small energy gap E_g, so a cooling system is necessary. Therefore, compound semiconductors such as CdTe are preferred because they can be used at room temperature and are

Table 2.1: Physical properties of the main semiconductors used as detectors.

Semiconductor	Si	Ge	CdTe
Atomic number	14	32	48/52
Density ($\mathrm{g\,cm^{-3}}$)	2.33	5.32	5.85
Energy gap E_g (eV)	1.12	0.665	1.5
Required average energy/single electron-hole pair ϵ (eV)	3.61	2.97	4.43
Mobility μ_e ($\mathrm{cm^2\,V^{-1}\,s^{-1}}$)	1500	3.6×10^4	1000
Mobility μ_h ($\mathrm{cm^2\,V^{-1}\,s^{-1}}$)	480	4.2×10^4	80
Lifetime τ_e (s)	3.0×10^{-3}	1.0×10^{-3}	1.0×10^{-6}
Lifetime τ_h (s)	3.0×10^{-3}	1.0×10^{-3}	1.0×10^{-6}

sensitive enough to X-rays above 100 keV, which are used in the diagnostic field. As mentioned above, while semiconductor detectors have the advantage of excellent energy resolution, they have the following disadvantages: 1) they are susceptible to noise in the readout circuitry at a later stage because they do not have internal amplification, 2) the depletion layer determines the sensitive area, making it difficult to enlarge the detector area, and 3) they have a longer dead time than scintillation detectors because of their small mobility and the time required to collect electron-hole pairs. In particular, the mobility of holes is small and their lifetime is short, so a large voltage must be applied to accurately collect their carriers.

2.2.2 Scintillation detectors

Scintillation detectors consist of a photodetector and a light-emitting material called a scintillator. The scintillator emits fluorescence when bombarded by radiation such as X-rays, γ-rays, or charged particles, and this fluorescence is used to detect X-rays. X-rays incident on the detector are converted to visible light inside the scintillator, which is then further converted to electric charge by a photodetector before being read out, so the energy resolution is generally lower than that of semiconductor detectors described in Section 2.2.1. Because of their detection methods, scintillation detectors are sometimes referred to as indirect conversion detectors and semiconductor detectors as direct conversion detectors. Both scintillators and photodetectors are available in a wide variety of types and can be combined to form a variety of scintillation detectors. In this section, we describe each scintillator, the photodiode (PD) used in clinical X-ray CT, the avalanche photodiode (APD), and the Multi-Pixel Photon Counter (MPPC), which has been the focus of much attention in recent years.

Scintillators are fluorescent materials that absorb the energy of radiation and immediately convert it into light, which can be roughly classified into organic and inorganic scintillators. The ideal scintillator should have high scintillation efficiency to convert radiation energy into fluorescence, a short time constant to obtain a high counting rate, transparency with respect to the wavelength of the generated light, and excellent light collection properties. However, no scintillator completely satisfies all of these performance requirements, so scintillators must be selected according to the desired detector characteristics.

Organic scintillators are classified into pure organic crystals such as anthracene, liquid scintillators, and plastic scintillators. Common advantages of organic scintillators include low cost, large area, short time constant, and excellent time response. On the other hand, due to their small density, organic scintillators have a very small reaction cross section for X-rays and γ-rays with a certain energy, and are therefore unsuitable for X-ray and γ-ray detection above 100 keV.

Compared to organic scintillators, inorganic scintillators have a higher atomic number value and are therefore sufficiently sensitive to high-energy X- and γ-rays. Thus, they are considered suitable for combination with diagnostic X-ray generators. The luminescence principle and required properties of inorganic scintillators are described below.

In the band structure model of inorganic crystals, all electrons are in an energy level called

the valence band. Between the valence band and the conductor, there is a region where electrons cannot exist (forbidden band). In inorganic crystals, this forbidden band (about 5–10 eV) is large, so electrons are not excited to the conductor at room temperature. When radiation strikes the crystal, the crystal atoms absorb the energy of the radiation and are excited, producing electrons and holes. Photons (visible light) are emitted when the electrons excited by the conductor transition to the ground level according to their lifetime. This is the process of converting radiation into visible light. Next, we discuss the performance requirements for scintillators.

1. Good conversion efficiency to fluorescence
   As mentioned in Section 2.2.1, in the case of X-ray and γ-ray measurements, the larger Z, the higher the probability of interaction (especially the photoelectric effect), and thus the higher the detection efficiency. Also, for the same size, the higher the density, the higher the detection efficiency.

2. Short decay time constant
   Scintillation emission decays exponentially with time. The decay time constant is directly related to the blind time of the entire detector. If a scintillator with a long decay time constant is used, it is difficult to obtain accurate measurements because even if new photons enter the detector during the decay time constant, they may be miscounted, or the energy information may be incorrectly acquired due to overlapping waveforms. Therefore, a scintillator with a short time constant is necessary, especially in high-counting-rate environments where waveform overlap is likely to occur.

3. The maximum emission wavelength matches the photo-detector's wavelength distribution of sensitized wavelengths
   The light photons produced by the scintillator must efficiently escape the scintillator and be transmitted to the next photosensor to be converted into an electrical signal. To this end, it is important that the maximum emission wavelength of the scintillator coincides with the wavelength distribution of the photosensors' sensing wavelengths.

A photodetector is used to convert X-rays converted into visible light inside the scintillator into electrical signals. There are various types of photodetectors, and here we describe the photodiode (PD), avalanche photodiode (APD), and multi-pixel photon counter (MPPC).

The principle of PD conversion from visible light to electrical signals is the same as that of semiconductor detectors. Compared to photomultiplier tubes, which have been conventionally used for radiation detection, PDs have a simpler structure, are more compact, have higher quantum efficiency, and exhibit less fluctuation due to photon statistics. On the other hand, the greatest drawback is that it is difficult to read out signals in pulses due to the lack of amplification and is vulnerable to noise from circuits and other sources. However, most detectors used in actual medical practice are a combination of a scintillator and PD, and diagnostic images are acquired by reading out signals from the photodiode in the current mode rather than the pulse mode.

APDs are semiconductor photodetectors with an internal amplification function, although the mechanism of photocurrent generation is the same as that of PDs. In a high electric field, carriers that collide with the crystal lattice generate new electron-hole pairs (ionization), and these electron-hole pairs undergo further ionization, resulting in repeated avalanche amplification. The amplification factor is 100 times. This internal amplification of the detector reduces the influence of circuit noise, and thus provides a superior signal-to-noise ratio compared to conventional photodiodes that do not have internal amplification. On the other hand, APDs have a temperature dependence, and the amplification factor changes as the temperature fluctuates even when a constant reverse bias is applied. Specifically, as the temperature increases, the amplification factor decreases because the lattice vibration of the crystal becomes more active and the electron-hole pairs collide with the crystal and lose velocity before gaining sufficient acceleration to generate secondary carriers. Therefore, to obtain a constant amplification factor, stable control of the reverse bias is required, taking into account the electric field intensity and temperature dependence.

The MPPC is a Sillicon photomultiplier (SiPM) detector developed by Hamamatsu Photonics. the MPPC consists of a Geiger-mode APD and a quenching resistor connected in series as one unit, which is connected in multiple parallel to form a two-dimensional array.

As mentioned above, normal APDs operate in linear mode, outputting an output charge proportional to the amount of incident light. However, the Geiger mode APD used in MPPC differs from this and is used when a certain voltage or higher is applied. When an APD is used in Geiger mode, a very high reverse bias is applied inside the device. When a photon is injected in this state, the generated electron-hole pairs are strongly accelerated, which generates new electron-hole pairs, resulting in the exponential generation of a large number of carriers. The multiplication factor at this time is about 10^{5-6}, which is much larger than the value of 100 times in the linear mode. As a result, Geiger mode APDs can generate discharge phenomena even for weak signals of a few photons.

The charge Q output during Geiger mode is constant regardless of the incident light level and is expressed by the following equation:

$$Q = C \times (V_{op} - V_{break}) \tag{2.10}$$

where C is the capacitance of the Geiger mode APD, V_{op} is the applied voltage, and V_{break} is the breakdown voltage. The charge Q from each parallel-connected pixel is integrated to form the overall MPPC signal. Since the output from each pixel is constant, the output itself does not contain the energy information of the incident photon. However, the higher the energy of the incident photon, i.e., the higher the light intensity, the greater the number of pixels to respond, so the final output from the MPPC will reflect the energy of the incident photon.

2.3 CT scanning type

The typical structure of a CT system consists of an X-ray tube and an X-ray detector placed in opposing positions, with the subject placed between them at the center and rotating around it. However, various scanning types have been created and clinically applied throughout its history. This section describes the characteristics of each scanning method and traces its evolution.

1. Translate/Rotate type (pencil beam type)
   This is also called the first-generation type because it was the first CT scanning system to be developed. As shown in Figure 2.3, it has one detector and the X-ray beam is thin and called a pencil beam. Scanning is performed by synchronous translation of the X-ray tube and detector, and is repeated at different angles. The use of a pencil beam eliminates the influence of scattered rays, but the scanning time is long. For this reason, it has been used exclusively for head scanning.

2. Translate/Rotate type (Narrow fan beam type)
   This type typically has about 10–20 detectors, and the X-ray beam is a narrow fan shape with a width of about $3-10^{\circ}$ (Figure 2.4). The angular interval of projection data acquisition can be done at each fan interval, which enables scanning in a shorter time (about 20 s) compared to the pencil beam method. This is called the second-generation method.

3. Rotate/Rotate type
   The X-ray beam is a fan beam that covers the entire object, and projection data is taken at once using detectors arranged in an arc (Figure 2.5). The scan can be completed simply by rotating the X-ray tube and detector as a single unit, without the need for translating motion as in conventional systems. The number of detector elements was initially 300, then increased to 700–1000 or more. Scanning time has been further shortened to a few seconds. This is the current mainstream of CT systems and is called the third-generation method.

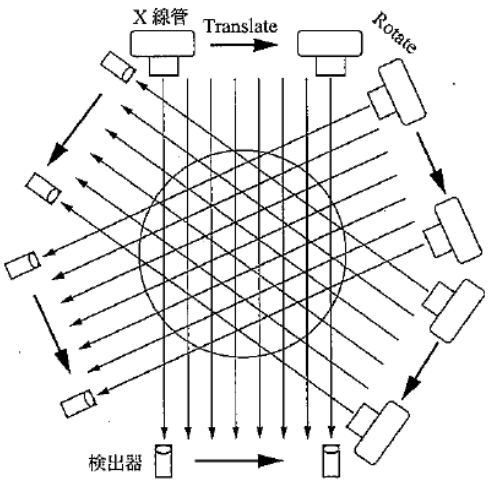

Figure 2.3: Translate/Rotate type (pencil beam type) [93].

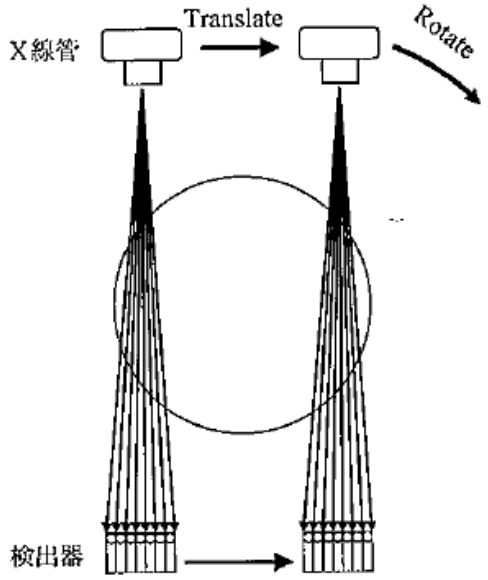

Figure 2.4: Translate/Rotate type (Narrow fan beam type) [93].

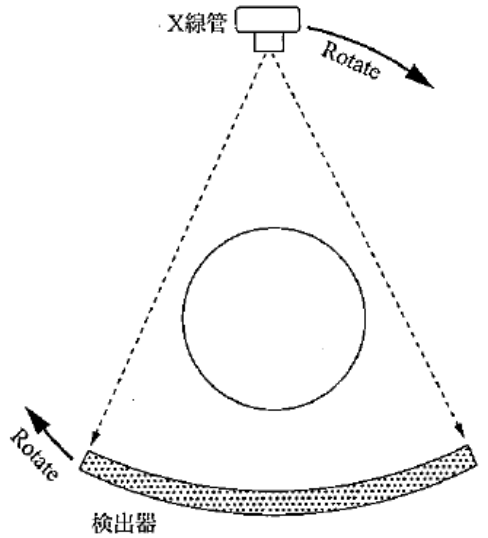

Figure 2.5: Rotate/Rotate type (fan beam type) [93].

2.4 Image reconstruction

Based on the X-ray intensity data collected by the CT scan, a CT image is created by the image reconstruction method [94]. In this section, we first consider what happens when X-rays enter the subject, and then describe how they are transformed into a CT image by image reconstruction.

2.4.1 Linear attenuation coefficient

The degree of X-ray attenuation is determined by the material-specific attenuation coefficient μ and the subject thickness t. Here, if the X-ray intensity reached in the absence of the subject is I_0 and the intensity after the subject is transmitted is I, the relationship between these two is expressed by the following equation:

$$I = I_0 \exp(-\mu t) \tag{2.11}$$

In general, the higher the density, the higher the μ (i.e., bone tissue has a higher μ relative to soft tissue). Also, the lower the X-ray energy (i.e., the lower the tube voltage), the higher the μ. In other words, the linear attenuation coefficient depends on the composition of the material and the X-ray energy. In a basic conventional CT scan, a tube voltage of about 120 kV is used, but since the X-ray energy is not changed significantly, μ at 55–65 keV, which is equivalent to the effective energy, is used as a reference.

2.4.2 Measured data and projection data

In considering image reconstruction, we define a coordinate system as in Eq. If the orthogonal coordinate system fixed to the subject is (x, y), then the distribution of the linear attenuation coefficients of the subject in this coordinate system is $f(x, y)$. Let (X, Y) be a new orthogonal coordinate system that shares the same origin and is rotated by an angle θ with respect to the coordinate system (x, y).

$$\begin{cases} x = X\cos\theta - Y\sin\theta \\ y = X\sin\theta + Y\cos\theta \end{cases} \tag{2.12}$$

Here, if an X-ray beam of intensity I_0 is irradiated parallel to the Y-axis, the X-ray intensity $I(X, \theta)$ after passing through the subject is as follows.

$$I(X, \theta) = I_0 \exp\left(-\int_{-\infty}^{\infty} f(x, y)dY\right) \tag{2.13}$$

This $I(X, \theta)$ is called the measurement data. The logarithmic transformation $g(X, \theta)$ of the attenuation rate of the X-ray intensity is expressed as

$$g(X, \theta) = \ln\left(\frac{I_0}{I(X, \theta)}\right) \tag{2.14}$$

$$= \int_{-\infty}^{\infty} f(x, y)dY \tag{2.15}$$

and is called the projection data. The operation of obtaining $g(X, \theta)$ from $f(x, y)$ is called the Radon transform. The projection data obtained in this way is given for all angles $0 \leq \theta \leq 2\pi$ around the subject, and the image reconstruction problem of X-ray CT is to find the distribution $f(x, y)$ of the linear attenuation coefficients of the subject from this distribution.

2.4.3 Projection-slice theorem

There are several analytical methods for obtaining the distribution $f(x, y)$ of the line attenuation coefficients of a subject from a set of projection data $g(X, \theta)$. Before that, we introduce the projection-slice theorem as an important theorem that forms the basis of image reconstruction. This clarifies mathematically the content of the image reconstruction problem.

First, as a two-dimensional reconstruction problem, let (ξ, η) denote the coordinates of the angular frequency of the frequency space corresponding to the real space (x, y), and let $F(\xi, \eta)$ be the two-dimensional Fourier transform of the distribution $f(x, y)$ of the linear attenuation coefficient of the subject. From the definition formula,

$$F(\xi, \eta) = \int_{-\infty}^{\infty} \int_{-\infty}^{\infty} f(x, y) \mathrm{e}^{-i2\pi(\xi x + \eta y)} dx dy \tag{2.16}$$

(ξ, η) expressed in the orthogonal coordinate system is transformed into the polar coordinate system (ω, θ),

$$\begin{cases} \xi = \omega \cos\theta \\ \eta = \omega \sin\theta \end{cases} \tag{2.17}$$

where ω is the angular frequency. Substituting Eq. 2.17 into Eq. 2.16,

$$F(\omega\cos\theta, \omega\sin\theta) = \int_{-\infty}^{\infty} \int_{-\infty}^{\infty} f(x, y) \mathrm{e}^{-i2\pi\omega(x\cos\theta + y\sin\theta)} dx dy \tag{2.18}$$

where $X = x\cos\theta + y\sin\theta$ and from the fact that the integral can be expressed as $dxdy = dXdY$,

$$\begin{aligned} F(\omega\cos\theta, \omega\sin\theta) &= \int_{-\infty}^{\infty} \int_{-\infty}^{\infty} f(x, y) \mathrm{e}^{-i2\pi\omega X} dX dY \\ &= \int_{-\infty}^{\infty} \left\{ \int_{-\infty}^{\infty} f(x, y) dY \right\} \mathrm{e}^{-i2\pi\omega X} dX \\ &= \int_{-\infty}^{\infty} g(X, \theta) \mathrm{e}^{-i2\pi\omega X} dX \\ &\equiv G(\omega, \theta)\,. \end{aligned} \tag{2.19}$$

where $G(\omega, \theta)$ represents the 1-D Fourier transform of the projection data $g(X, \theta)$ in the X direction. From Eq. 2.19, we see that the component in the direction of a certain angle θ in the 2-D Fourier transform of the distribution of line attenuation coefficients $f(x, y)$ that we want to find is equal to the 1-D Fourier transform of the projection in the same θ direction. This is called the projection-slice theorem, and by obtaining the projection data $g(X, \theta)$ for $0 \leq \theta \leq \pi$, the Fourier transform $F(\xi, \eta)$ of $f(x, y)$ is completely determined. Thus, the distribution $f(x, y)$ of the linear attenuation coefficients of the subject is obtaied by Eq. 2.20, which is the 2-D Fourier inverse transform of $F(\xi, \eta)$.

$$f(x, y) = \int_{-\infty}^{\infty} \int_{-\infty}^{\infty} F(\xi, \eta) \mathrm{e}^{i2\pi(\xi x + \eta y)} d\xi d\eta \tag{2.20}$$

2.4.4 2D Fourier transform method

The 2-D Fourier transform method uses Eq. 2.20 as is to reconstruct the image. In this method, the only specific calculations are those for the 1-D and 2-D Fourier transforms, both of which are performed extremely quickly using the Fast Fourier Transform (FFT). However, considering a digital computation by a concrete computer, the positions of the grid points (ω_i, θ_j) in the polar coordinate representation of $F(\omega\cos\theta, \omega\sin\theta)$ in Eq. 2.19 and the grid points (ξ_m, η_n) in the orthogonal coordinate representation of $F(\xi, \eta)$ in Eq. 2.20 are generally different, so an appropriate interpolation calculation is necessary. In this case, if the accuracy of the calculation is not sufficient, artifacts based on errors will occur.

2.4.5 Filtered backprojection (FBP)

The Filtered Back-Projection (FBP) method is an analytical method that is mathematically equivalent to the two-dimensional Fourier transform method described above. Here, Eq. 2.20 is expressed

in polar coordinates instead of orthogonal coordinates to avoid errors caused by interpolation calculations. Using Eq.2.17 to express Eq. 2.20 in a polar coordinate system with radial direction ω and angular direction θ, the integral is $d\xi d\eta = \omega d\omega d\theta$, so we have

$$\begin{aligned} f(x,y) &= \int_{-\infty}^{\infty}\int_{-\infty}^{\infty} F(\xi,\eta)\mathrm{e}^{i2\pi(\xi x+\eta y)}d\xi d\eta \\ &= \int_{0}^{2\pi}\int_{0}^{\infty} F(\omega\cos\theta,\omega\sin\theta)\mathrm{e}^{i2\pi\omega(x\cos\theta+y\sin\theta)}\omega d\omega d\theta \\ &= \int_{0}^{\pi}\int_{-\infty}^{\infty} F(\omega\cos\theta,\omega\sin\theta)|\omega|\mathrm{e}^{i2\pi\omega(x\cos\theta+y\sin\theta)}d\omega d\theta \\ &= \int_{0}^{\pi}\left\{\int_{-\infty}^{\infty} G(\omega,\theta)|\omega|\mathrm{e}^{i2\pi\omega X}d\omega\right\}d\theta\,. \end{aligned} \tag{2.21}$$

Here

$$\begin{aligned} q(X,\theta) &\equiv \int_{-\infty}^{\infty} G(\omega,\theta)|\omega|\mathrm{e}^{i2\pi\omega X}d\omega \\ &= \int_{-\infty}^{\infty}\left\{\int_{-\infty}^{\infty} g(X,\theta)\mathrm{e}^{-i2\pi\omega X}dX\right\}|\omega|\mathrm{e}^{i2\pi\omega X}d\omega\,, \end{aligned} \tag{2.22}$$

$q(X,\theta)$ means that the 1-D Fourier transform $G(\omega,\theta)$ of the projection data $g(X,\theta)$ in the angle θ direction to X is multiplied by the filter represented by $|\omega|$ in the domain of frequency ω, and then transformed back by the Fourier inverse transform. This corresponds to the "F (Filtered: filter correction)" part of FBP. Using $q(X,\theta)$ to express the rest of the equation, we obtain

$$\begin{aligned} f(x,y) &= \int_{0}^{\pi} q(X,\theta)d\theta \\ &= \int_{0}^{\pi} q(x\cos\theta+y\sin\theta,\theta)d\theta\,. \end{aligned} \tag{2.23}$$

This corresponds to the "Back Projection (BP)" part of FBP. The FBP is the most basic reconstruction method in current CT systems. Filtering (1D) of the projection data is advantageous because it can be done very quickly in frequency space using the FFT, as is already common practice in general data processing. For this reason, the FBP, which performs filtering in frequency space, has become the basic algorithm for diagnostic CT.

Chapter 3

Contrast-enhanced CT imaging using photon-counting CT

In this section, we give an overview of our photon-counting CT and its performance, based on papers [47, 95]. To realize the PC-CT system, we first fabricated an X-ray detector that combines a scintillator and MPPC. To read X-ray signals from this detector at high speed, we designed our signal processing system and implemented it on a Large Scale Integration (LSI) circuit and an LSI evaluation board.

3.1 Materials

The detector utilized in this experiment was assembled by optically coupling SiPMs and scintillation crystals. The SiPM employed was a multi-pixel photon counter (MPPC) manufactured by Hamamatsu Photonics K.K., while the scintillator consisted of cerium-doped yttrium-gadolinium-aluminum-gallium garnet (YGAG:Ce, Proterial Ltd.) (see Fig. 3.1). The specifications of the detector are outlined in Table 3.1, a linear array type X-ray detector with $1 \times 1 \times 1$ mm scintillator per channel and 1×1 mm MPPC photosensitive surface, for a total of 64 channels. Thus, the total length is approximately 64 mm. This is a size that roughly covers the entire body of a small animal, such as a mouse, for example.

3.2 Readout system

Figure. 3.2 shows an overview of the large-scale integrated circuit (LSI) we have developed and its internal circuit configuration [95]. The left side of the Fig. 3.2 shows the circuit configuration per

Table 3.1: Characteristics of SiPM-based PC detector [90].

Characteristics	Our SiPM-based PC detector
Overall detector characteristics	
Detector shape	linear array
Number of channels	64
Channel size (mm^2/channel)	1×1
Maximum counting rate (counts/s/mm^2)	$\sim 4.0 \times 10^6$
YGAG:Ce (Scintillation crystal)	
Voxel volume (mm^3/channel)	$1 \times 1 \times 1$
Decay time constant (ns)	$\sim$70
MPPC (SiPM)	
Pixel size (mm^2/channel)	1×1
micro-cell size (μm/pixel)	25

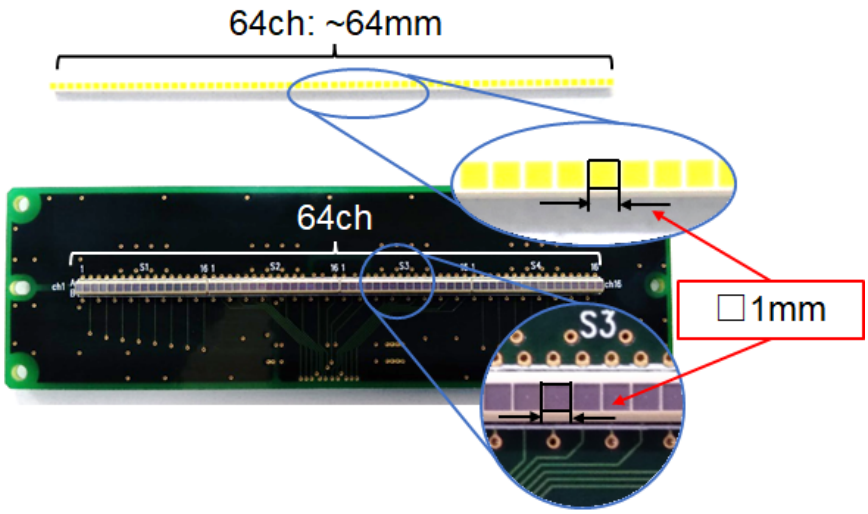

Figure 3.1: 64-channel linear array detector consists of two main components. Top: YGAG:Ce scintillators. Bottom: MPPCs. These components are optically bonded together and have the capability to convert X-rays into electrical charge [47].

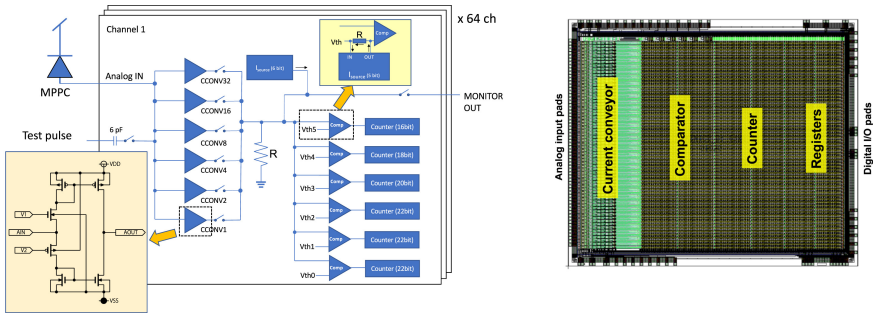

Figure 3.2: Large-scale integrated circuit (LSI) we developed [95]. Left: Circuit configuration inside the LSI. This configuration is for one channel, and there are 64 channels inside the LSI. Right: Overall view of the LSI.

channel inside the LSI, which has 64 channels in total. charge signals from the MPPC are gain-adjusted by an amplifier. To achieve high-speed signal processing, a current conveyor circuit, which can be designed to have low input impedance and high output impedance, is used in the amplifier. The signal passing through the amplifier is converted from a charge pulse to a voltage by a resistor in the subsequent stage. The height of this voltage signal is compared with the threshold voltage of six comparators, and only the signals exceeding the threshold are counted by the counters in each subsequent stage; in the case of X-ray signals, the signal height is proportional to the energy of the X-rays, so it is possible to simultaneously measure the number of X-rays and their energy.

Before evaluating the performance of CT imaging, the performance of the fabricated X-ray detector was evaluated. The measured performance is summarized in Table. 3.2 [95].

Table 3.2: Performance of our photon-counting detector.

Performance	
Signal linearity (mA)	0–1.0
Energy resolution (%, FWHM @ 59.5 keV)	40.5 ± 1.5
Deadtime (ns)	247 ± 4
Maximum countable count rate (MHz)	~ 4.0

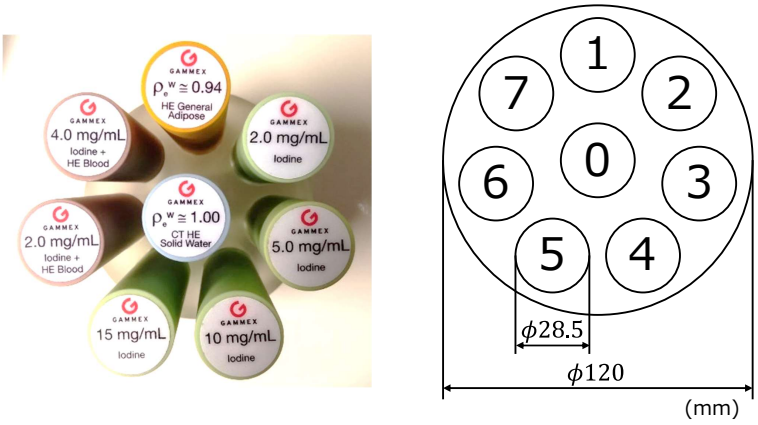

0	1	2	3	4	5	6	7
Water	Adipose	Iodine 2.0	Iodine 5.0	Iodine 10.0	Iodine 15.0	Iodine 2.0 + Blood	Iodine 4.0 + Blood

(mg/mL)

Figure 3.3: Static phantom. Left: Gammex™ Technology rod phantoms are inserted into a cylindrical jig made of PMMA. Right: Each numbered position corresponds to a rod phantom equivalent to water, fat, iodine, etc. in the lower table. [47].

3.3 CT imaging performance

3.3.1 Subjects for CT imaging

In vivo contrast agents travel throughout the body in the bloodstream. Therefore, to evaluate CT imaging performance under conditions where the contrast agent does not move, a Multi-Energy CT Phantom model (manufactured by Gammex™ Technology), which is widely used in clinical practice, was first prepared as the subject (Fig. 3.3). This stick-shaped static phantom well simulated contrast agents, water, and adipose. They were inserted into a proprietary acrylic (PMMA) cylindrical jig and fixed in position during CT imaging.

To evaluate the performance of the originally developed PC-CT for clinical application, a mouse model (approximately 100 mm long) was prepared (Figure 3.4). The mouse was pre-anesthetized and inserted into a cylindrical Styrofoam container to prevent movement. Subsequently, 0.2 mL of iodine-containing contrast agent was injected intravenously through the tail. CT imaging was then performed on the mouse model twice at intervals: immediately and 2 hours after injection.

3.3.2 Geometric configuration with X-ray generator

The experimental setup of the established PC-CT system is illustrated on Fig. 3.5. A first-generation CT scanning system was developed by vertically installing and fixing a linear array of the custom PC detector [95], with the X-axis stage—where the subject was positioned—moving perpendicular to the X-ray beamline. X-rays emitted from the X-ray generator are suppressed on the low energy side by a 1.5 mm thick aluminum filter (see Fig. 2.1). Since the arrival rate of X-rays is higher on the low energy side, the probability of multiple X-ray signals coming in almost simultaneously increases. As a result, the number of X-rays is counted off, which affects the attenuation intensity distribution of the material on the CT image. This deteriorates the accuracy of substance identification and concentration estimation and should be prevented as much as possible. After passing through the subject, the intensity is measured by a 64-channel X-ray detector; a copper block is placed in front of the X-ray detector to reduce the scattering component of the X-rays. X-ray signals from the detector were converted from analog to digital signals by the proprietary LSI [95].

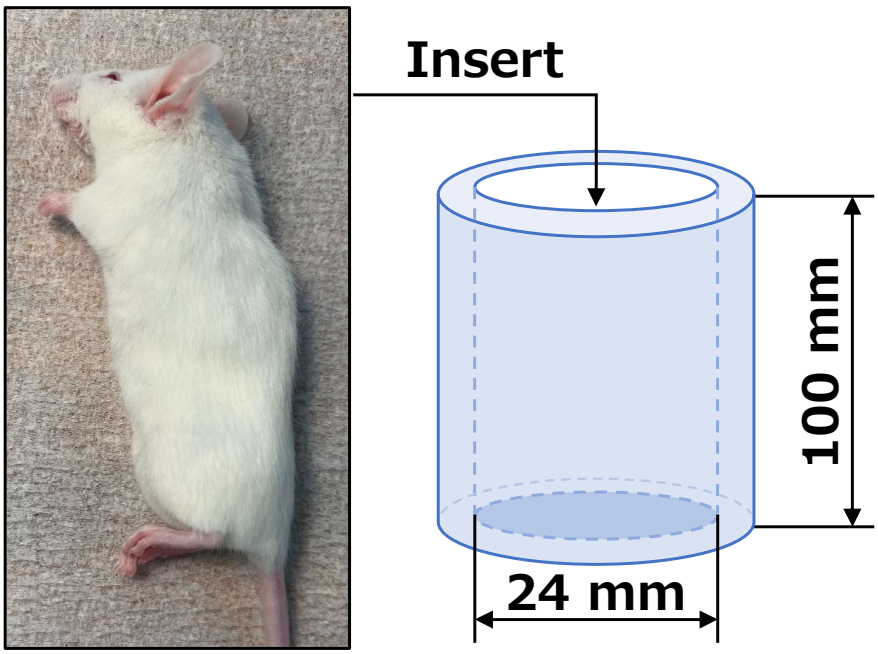

Figure 3.4: Mouse model inserted into a cylindrical Styrofoam container [47]. The mouse is put to sleep by anesthesia and does not move within the cylindrical container.

The CT images were subsequently generated using a classical image-reconstruction algorithm (FBP, Fig. 3.6). The following briefly reiterates the FBP (see section 2.4.5 for detailed equations). The data measured by CT imaging is formed into a sinogram by forward projection and logarithmic transformation. The sinogram is the data aligned with the X-ray detection position on the horizontal axis and the rotation angle on the vertical axis. It is then 1D Fourier transformed and passed through a typical filter that reduces low-frequency components, called a ramp filter. The filtered data is further returned to real space by an inverse Fourier transform, and finally back-projection completes the image reconstruction. Six energy thresholds are set inside the LSI and the values can be changed arbitrarily; up to six CT images can be made without overlapping energy bands. Other conditions of the experiment are shown in Table 3.3.

Table 3.3: Experimental setup for PC-CT imaging on each subject.

Parameters	Static phantom	Mouse model
X-axis movement step / total amount (mm)	1 / 130	1 / 34
CT rotation angle step / total amount (°)	0.9 / 180	3.75 / 180
Number of projections	200	48
Total CT imaging time (min.)	1020	25
Tube voltage / current (kV/mA)	120 / 0.1	100 / 0.5
Weighted CT dose index (mGy)	10	4.1
Energy threshold (keV)	11.2, 33.2, 55.2, 65.0, 75.0, 90.0	23.2, 33.2, 50.2, 60.0, 75.0, 90.0

3.3.3 Iodine K-edge imaging

From this section 3.3.3, we present the methods used to analyze the obtained CT images. First, K-edge imaging, a conventional contrast enhancement technique, is presented in this section 3.3.3, followed in the next section 3.3.4 by the concentration mapping used in this study.

K-edge imaging is a valuable technique for identifying materials, allowing for the visualization of specific substances based solely on their X-ray energy characteristics [96–99]. Notably, iodine

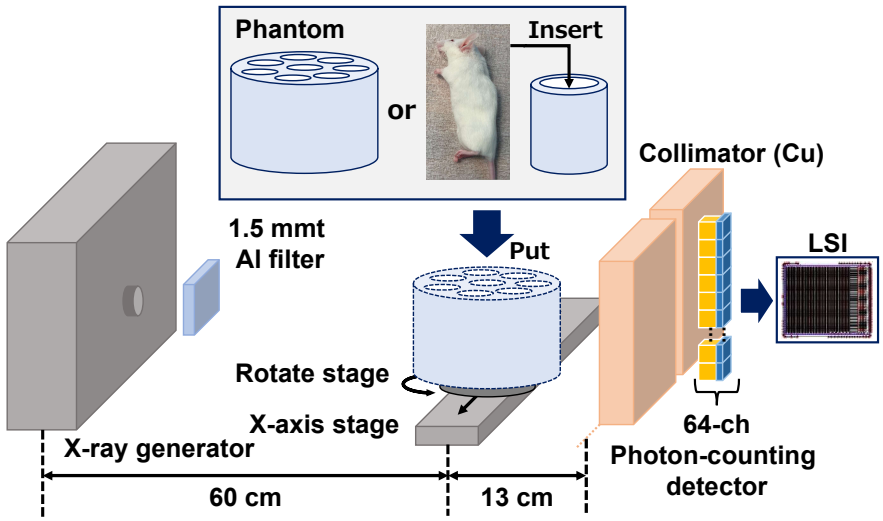

Figure 3.5: CT imaging setup with our established SiPM-based PC-CT system [47]: X-rays emitted from the X-ray generator are suppressed on the low-energy side by a 1.5-mm-thick aluminum filter. After passing through the object, the intensity is measured by a 64-channel X-ray detector. A copper block is placed in front of the X-ray detector to reduce the scattering component of the X-rays.

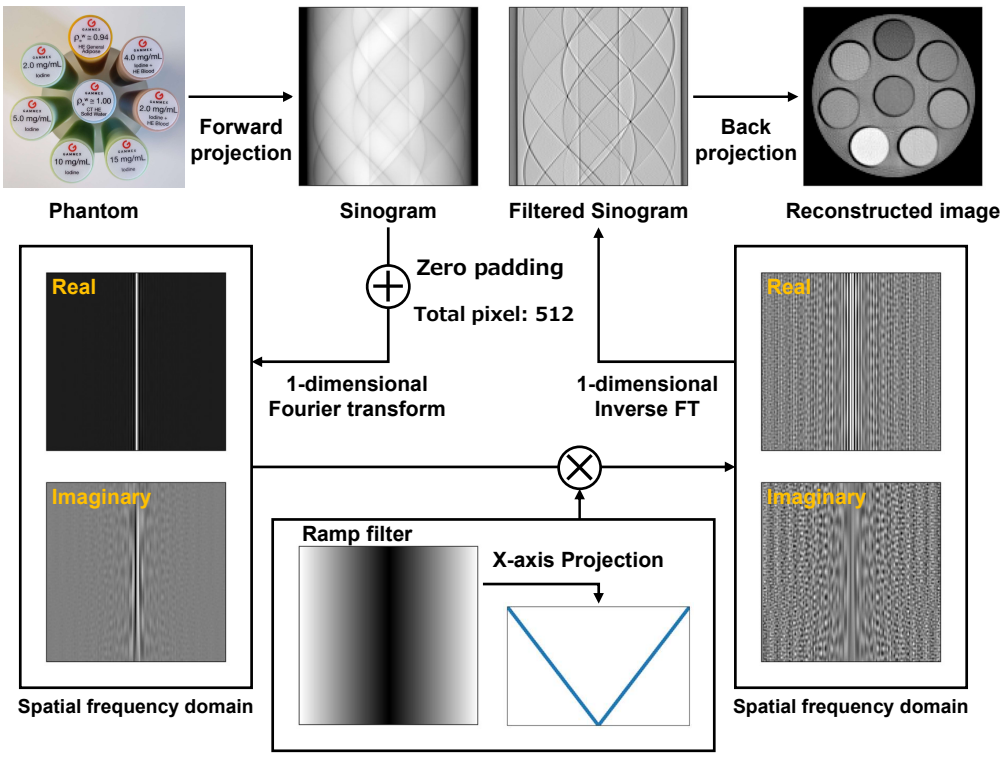

Figure 3.6: Filtered back-projection method. This is a classical image reconstruction technique.

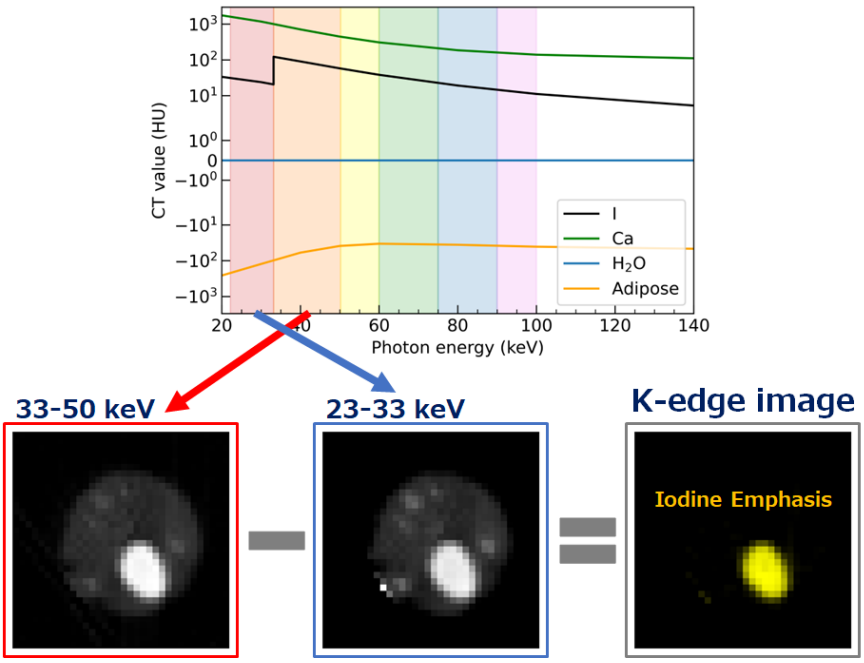

Figure 3.7: Overview of iodine K-edge imaging. Top: CT values of iodine, the main component of iodine contrast agent, and various substances present in the human body plotted against X-ray energy. With the exception of iodine, CT values show smooth transitions in the energy range of 20–120 keV. Bottom: CT images of the abdomen of a model mouse with energy bands of 33–50 keV and 23–33 keV and an iodine K-edge image produced by subtracting these images [47].

exhibits a unique K-edge absorption at 33.2 keV, leading to a distinct change in the mass attenuation coefficient at this energy level. In contrast, the mass attenuation coefficients of other biological tissues, such as water, adipose tissue, bone, and soft tissue, gradually decrease as energy increases within the range of 20 to 120 keV. Here, we introduce the CT value, which is the pixel value of a CT image commonly used in clinical practice:

$$CT\,(\mathrm{HU}) = 1000 \times \frac{\mu_t - \mu_w}{\mu_w} \tag{3.1}$$

where μ is the linear attenuation coefficient, a value expressed as the product of the density of the substance and its mass attenuation coefficient. In addition, the subscripts t and w are the target substance and water, respectively. Since the CT value is a dimensionless quantity, HU (Hounsfield Units) are used as the unit of measure for convenience. the CT value is used because the linear attenuation coefficient varies depending on the clinical equipment and imaging conditions, and CT images taken under different conditions are not comparable. The CT values normalized by air and water can be used for comparison. Therefore, it is currently most appropriate to use CT values in CT images.

When deriving CT values for different materials, only the CT value of iodine shows a notable discontinuity at 33.2 keV (see the top panel of Fig. 3.7). Based on the facts, the K-edge image of iodine can be generated as follows: subtract the value of each voxel in the CT image corresponding to an X-ray event with an energy lower than the K-absorption edge of iodine from the CT image in the higher energy band. This alone produces an image that highlights the presence of iodine, known as the iodine K-edge image. Since our device has more than three energy thresholds, it is possible to acquire CT images in two energy bands. In other words, by setting the threshold appropriately, CT images in energy bands lower or higher than the K-edge can be acquired, allowing K-edge imaging. In our study, we applied K-edge imaging to visualize the spatial distribution of iodine in vivo, as depicted in the bottom panel of Fig. 3.7.

3.3.4 Concentration mapping with six energy bands

K-edge imaging, illustrated in Fig. 3.7, amplifies the signals of specific materials. However, this technique lacks the ability to provide quantitative values such as the the concentration of contrast agents. While conventional K-edge imaging typically involves subtracting two CT images with haigher and lower energy bands than that of K-edge of the target materials, our system expands this capability to six energy bands, enabling additional information to complement material visualization. By collecting multiple CT images of the target material across various energy bands, we can not only visualize the emphasis of the materials but also estimate their concentrations [45, 46]. Consequently, in this study, we estimated the iodine concentration using the all six energy bands, a feature not present in traditional CT systems. The algorithm employed for concentration determination is based on the least-squares method, with the relevant equation expressed as:

$$J = \sum_{E=1}^{6} \left(\mu_{measured,E} - \rho_t \cdot \mu_{t,E}\right)^2 \tag{3.2}$$

where $\mu_{measured,E}$ represents the measured linear attenuation coefficient for a given energy band E, ρ_t denotes the concentration of the target material, and $\mu_{t,E}$ stands for the mass attenuation coefficient obtained from a database called XCOM of NIST [100] as a known value. Therefore, the concentration of the target is obtained by calculating the least squares method with rho as the unknown.

In this study, we employed multiple energy bands to distinguish between materials in each static phantoms and a mouse model and to estimate iodine concentrations (Fig. 3.7, Top). Specifically, we examined the same mouse model as in the K-edge imaging section (Section 3.3.3). By utilizing a greater number of CT values across various energy bands, which can more precisely track attenuation coefficients dependent on X-ray energy, we incorporated all six energy bands (23–33 keV, 33–50 keV, 50–60 keV, 60–75 keV, 75–90 keV, 90–100 keV) to improve the accuracy of concentration estimates [46]. The energy band width was set to approximately 10–20 keV, taking into account the detector energy resolution.

To generate an iodine concentration map for the mouse model, we categorized the pixels of the CT images into three groups: iodine-dominant organ/tissue, soft tissue including adipose, and bone (calcium), with typical CT values ranging from -70 to 70 HU for soft tissue, -400 to -200 HU for adipose and 300 to 1000 HU for bone. Initially, we obtained the CT images of the mouse model in the six energy bands. Subsequently, if the CT values obtained were lower than approximately 100 HU across all six energy bands, the corresponding voxel was deemed to represent soft tissue or adipose because the maximum CT value of soft tissue is typically 100 HU. In such cases, the iodine concentration map in the corresponding voxel was set to 0 mgI/mL.

On the contrary, voxels displaying CT values higher than those observed for soft tissue were interpreted as potentially containing calcium or iodine-rich soft tissue/organs. We replaced the mass attenuation coefficient of either iodine or calcium for the parameter $\mu_{t,E}$ in Equation 3.2. When fitting the obtained CT values of a voxel of interest with Equation 3.2, we selected a scenario with a smaller J, allowing for an estimation of concentration as well as material identification only after confirming the presence of iodine or calcium beyond doubt.

Ultimately, if a voxel primarily indicated the presence of iodine, we utilized the iodine concentration derived from Eq. 3.2 for the concentration map. Conversely, if a voxel predominantly indicated the presence of calcium, we assigned it a zero iodine concentration (Fig. 3.8).

In addition, concentration mapping was performed by correcting iodine concentration values in vivo in mice from the results obtained from the static phantom analysis (see next section 3.3.5).

3.3.5 Results and discussion of static phantom imaging

Here we present the results of CT imaging of static phantoms. First, CT images of the static phantom are shown in Fig. 3.9. It can be seen that iodine has different CT values for each energy band. Next, to verify the validity of the obtained CT images, the CT values of each iodine obtained

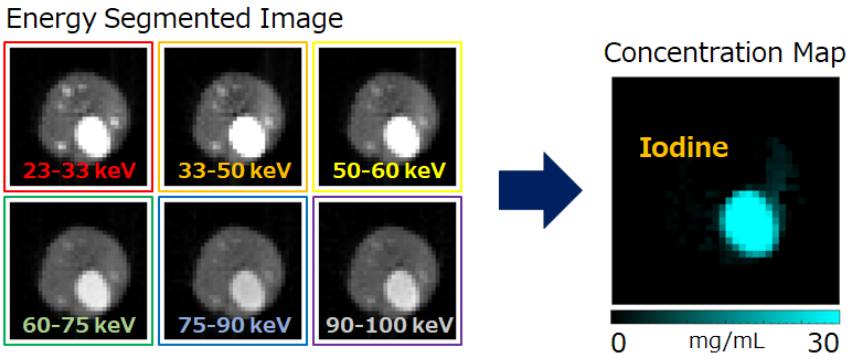

Figure 3.8: Overview of concentration mapping. Left: CT image of mouse abdomen injected with iodine contrast agent; CT images were produced in six energy bands. Right: iodine concentration map using Eq. refeq:LSM. Not only iodine is highlighted, but even its concentration distribution can be quantitatively shown [47].

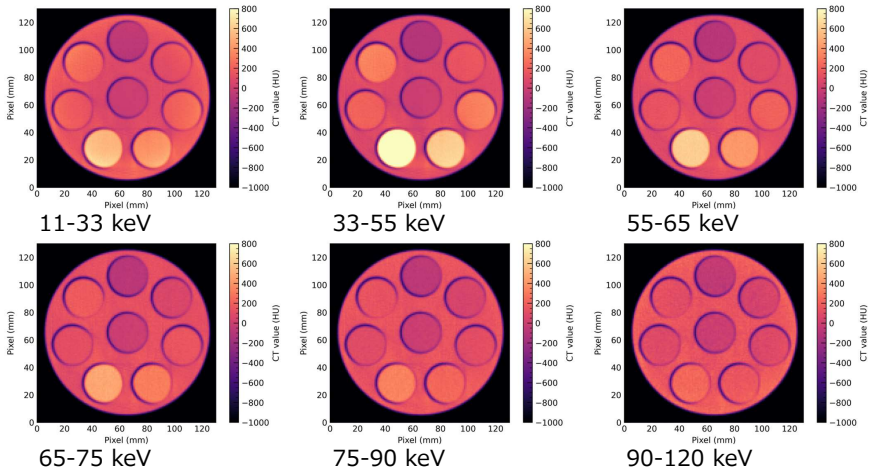

Figure 3.9: Measured CT images of the static phantom.

from the experiment are compared with the ideal values obtained by simulation. The following is a description of how to create ideal values by simulation:

1. obtain mass attenuation coefficients (I, H2O, Adipose, PMMA) from a database (XCOM from NIST [100]), create numerical images, and obtain X-ray count maps using forward projection and log transformation (Fig. 3.10).

2. assume the spectrum and the energy resolution of the detector and act on the X-ray count map. The energy spectrum is assumed to be the characteristic X-ray of tungsten and continuous X-ray due to bremsstrahlung. The energy resolution at each energy is calculated from the previously measured value of ^{241}Am (∼40%@59.5 keV) and is applied to the count map (Fig. 3.11).

3. compare the obtained simulated images with the experimentally obtained CT images (Fig. 3.12).

The results of the comparison of CT values between the ideal CT image obtained by the above simulation and the CT image obtained by the measurement are represented in Fig. 3.13. The Fig. 3.13 shows each CT value in the region where 2 mg/mL of iodine is present. The region (region of interest, ROI) is set at 10 × 10 pixels. Here, the gray curve is the CT value calculated using the mass attenuation coefficient obtained by XCOM in NIST [100], and the purple and green dots are obtained from simulation; the purple dots are CT values calculated for each 1 keV, and the green dots are CT values calculated for each energy band used in the experiment. The

Figure 3.10: Simulation method (#1). Numerical images are obtained and then Count maps are obtained using the forward projection and the log transformation.

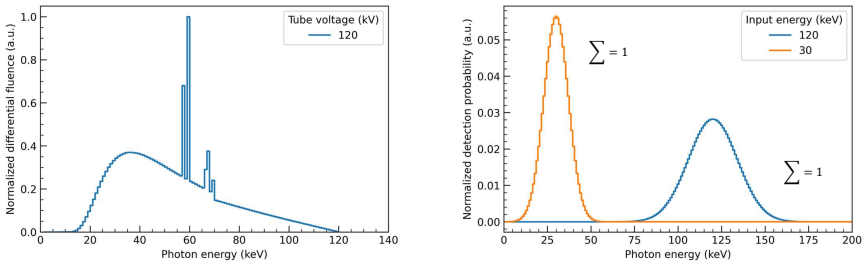

Figure 3.11: Simulation method (#2). Left: Incident X-ray spectrum. Right: Energy resolution of the detector.

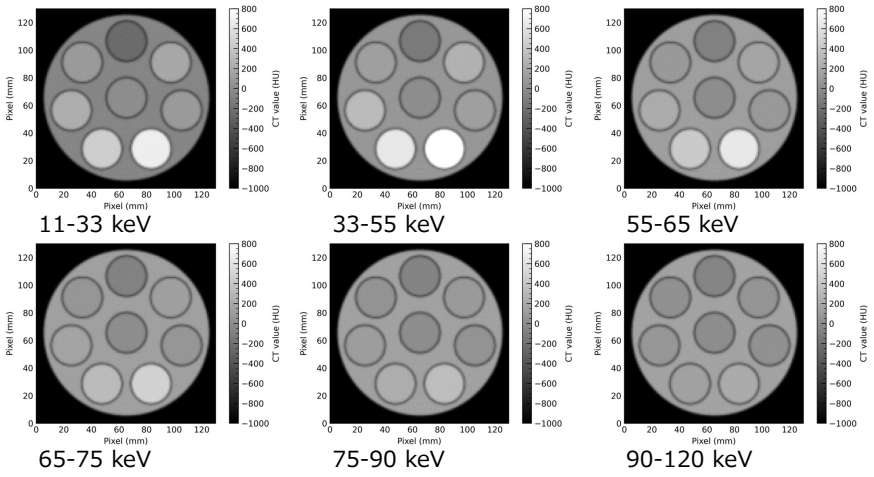

Figure 3.12: Simulation method (#3). Ideal CT images obtained from simulation.

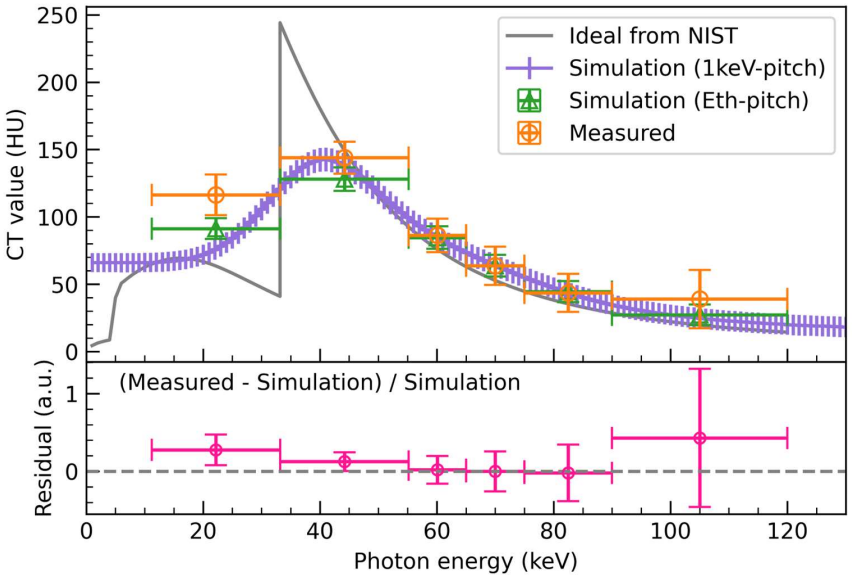

Figure 3.13: Energy dependence of CT values for 2 mg/mL of iodine. Gray curves are ideal values obtained from NIST XCOM. Purple and green plots are values obtained by simulation. The orange plots are values obtained from measurements.

orange dots represent the measured values. The residuals between the simulations (green) and the measurements (orange) are shown as pink dots at the bottom of the Fig. 3.13. From the residuals, it can be confirmed that they generally agree within the margin of error. Similarly, the residuals between the simulated and measured values for the other iodine concentrations (5, 10, and 15 mg/mL) show that they are generally in agreement within the margin of error for all concentrations (Fig. 3.14).

Next, iodine concentration mapping of the static phantom was performed and the results are shown in Fig. 3.15. Static phantoms equivalent to water and fat were inserted in the center and 12 o'clock directions of the Fig. 3.15, respectively, but since they do not contain iodine, the concentration map shows 0 mg/mL, which is correctly estimated as expected. On the other hand, the estimated concentration of each iodine is compared with the ideal value of XCOM [100] to evaluate the accuracy of the estimation. For the estimated iodine concentration map, a 10 $\times$ 10 pixel ROI was set at the iodine position for each concentration, and the mean and standard deviation were calculated. The Fig. 3.16 shows this compared to the ideal value. The blue dots are the concentrations obtained from the measured data. The iodine concentration estimated from the simulated data is also shown as orange dots. The residuals at the bottom of the Fig. 3.16 show that the simulated concentrations are consistent with the ideal values in the range 2–15 mg/mL. The measured concentrations are also found to be roughly in agreement around 2–10 mg/mL. On the other hand, the residuals at 15 mg/mL clearly deviate from the ideal values. Therefore, it is necessary to consider a correction to correctly estimate the concentration of iodine contrast agent.

Here, we discuss the causes of the deterioration in the accuracy of concentration estimation at high concentrations. PC-CT counts the number of incident X-rays, but miscounting occurs when the frequency of incident X-rays events is high. For example, consider the case where two X-ray events arrive almost simultaneously, as shown in the Fig. 3.17. That is, the first X-ray event arrives 100 ns after the start of observation, and the second arrives 70 ns after that. The first event can be measured as one event without any problem, along with its wave height value (proportional to the X-ray energy). However, the originally developed X-ray detector used in this study has a dead time of approximately 250 ns, so no matter how many X-ray events arrive during that time, they cannot be counted. Therefore, the second event is miscounted. This miscounting is more likely to occur at higher X-ray irradiation rates (i.e., before the X-rays penetrate the subject). On the other hand,

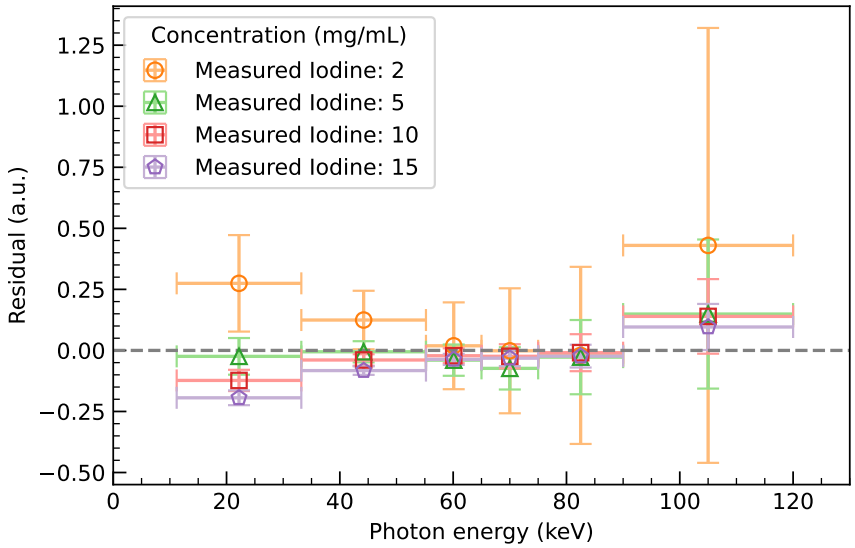

Figure 3.14: Residuals of measured and simulated CT values at various concentrations. The fact that they are generally consistent at all concentrations indicates that the measurements were performed correctly.

after the X-rays penetrate the subject, the rate is relatively low because the X-rays are attenuated. In particular, when comparing the same material and thickness, the higher the concentration, the greater the attenuation of the X-rays, and thus the lower the arrival rate. In other words, the higher the concentration, the lower the X-ray count error after transmission through the subject. The above can be expressed using a mathematical formula as follows. First, the calculation of the amount of X-ray attenuation, which is performed in the first step to obtain a CT image, is shown below:

$$Amount\,of\,attenuation = -\log\left(\frac{I}{I_0}\right) \tag{3.3}$$

where I_0 is the X-ray count before the subject transmission and I is the X-ray count after the subject transmission. Next, assume a situation in which a sufficiently high-density subject is to be imaged by CT. Let $I_{0,Ideal}$ be the pre-transmission count under the ideal situation with no miscounting, $I_{0,misscount}$ be the pre-transmission count where miscounting occurs, I_{Ideal} be the post-transmission count under the ideal situation with no miscounting, and $I_{misscount}$ be the post-transmission count where miscounting occurs, then $I_{0,Ideal} > I_{0,misscount}$ and $I_{Ideal} \sim I_{misscount}$ are valid, so the attenuation is as in the following inequality:

$$-\log\left(\frac{I_{Ideal}}{I_{0,Ideal}}\right) \gtrsim -\log\left(\frac{I_{misscount}}{I_{0,misscount}}\right) \tag{3.4}$$

Thus, the higher the concentration, the lower the apparent concentration because the X-ray attenuation is lower than the ideal value. Since this naturally affects concentration estimation, a simple correction for concentration is made using the Power-Law model, in which the higher the concentration, the lower the value. Here, fitting is performed by Power-Law for the relationship between the measured and ideal values in Fig. Power-Law is expressed by the following equation:

$$y = ax^b + c \tag{3.5}$$

where y is the value on the vertical axis, x is the value on the horizontal axis, and a, b, and c are variables. The results of the fitting are as follows: $a = 1.06 \pm 0.22$, $b = 0.94 \pm 0.07$, and $c = 0.12 \pm 0.43$. The fitting errors for each variable indicated that the fitting was sufficiently

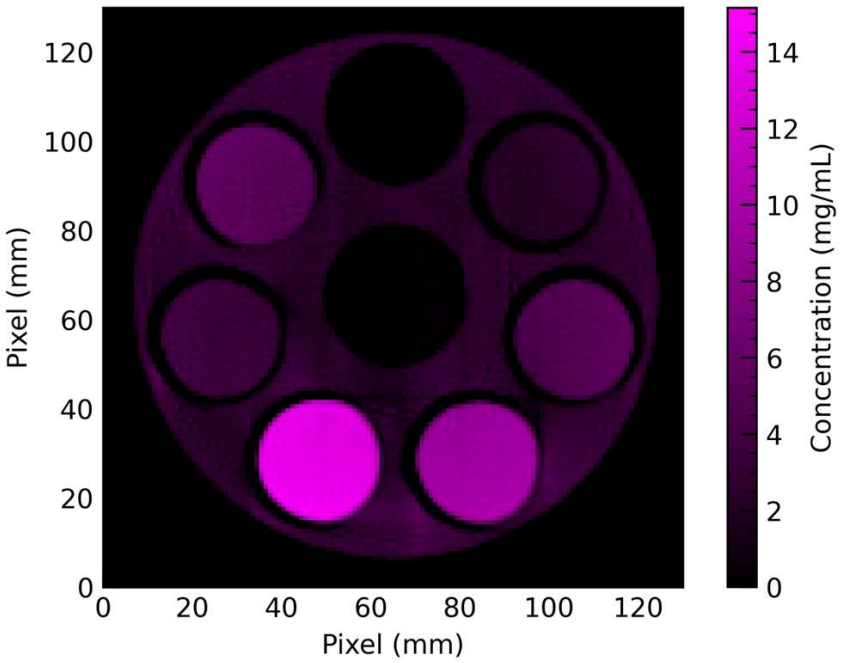

Figure 3.15: Iodine concentration map of the static phantoms.

accurate. Power-Law and these variables will be used to apply to the concentration estimation results presented in the subsequent analysis of mice.

3.3.6 Time-series concentration map of in vivo

Following this, concentration maps were generated based on the six CT images acquired prior to iodine injection, 30 minutes post-injection, and 2 hours post-injection, respectively. Figs. 3.18 and Fig. 3.19 exhibit the CT images utilizing X-ray events within the 23–100 keV energy band (equivalent to conventional CT images), along with concentration maps and overlay images (i.e., CT images + concentration maps) of the abdomen and chest, respectively, at various time points post-injection. These visual representations distinctly delineate temporal and spatial fluctuations in iodine concentrations within the mouse model's biological tissues or organs.

As depicted in the conventional-like CT images in Fig. 3.18, prior to iodine injection, the spine and leg bones exhibit high CT values (approximately 1000 HU), while soft tissues and adipose display CT values similar to water (approximately 0 HU). Remarkably, the CT images acquired 30 minutes and 2 hours after injection reveal significantly higher CT values in the bladder compared to other areas (approximately 2700 HU in the bladder). In clinical X-ray CT systems utilizing energy-integrating detectors, such elevated CT values in the bladder are commonly associated with the administration of an iodine contrast agent, based on both pre-injection and post-injection CT images. However, the concentration map allows one to conclude that the bladder enhancement is due solely to the iodine contrast agent based solely on the post-injection images without the pre-injection images. Furthermore, in Fig. 3.19, we could not distinguish iodine from bone in conventional CT images acquired with a single energy band, but the concentration map clearly shows iodine accumulation in the kidney. Our PC-CT system solved these drawing limitations by utilizing multiple energy bands, allowing us to effectively distinguish various biological tissues.

From here, we show the average iodine concentration in each tissue in the obtained iodine concentration map. At 30 minutes after injection, the iodine accumulated in the bladder averaged about 93.5±9.9 mgI/mL, but after 2 hours, it was found to have decreased to 67.4±7.9 mgI/mL. Also, in the kidneys, the dose was 39.3±5.0 mgI/mL at 30 minutes after injection, but was approximately 5 mgI/mL at 2 hours after injection. This trend aligns with the findings of K-edge imaging

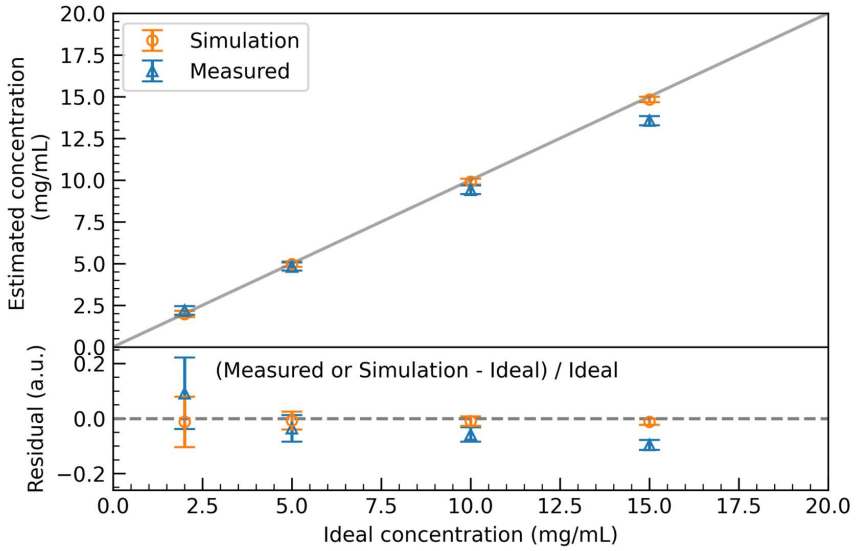

Figure 3.16: Measured or simulated vs ideal concentration of iodine.

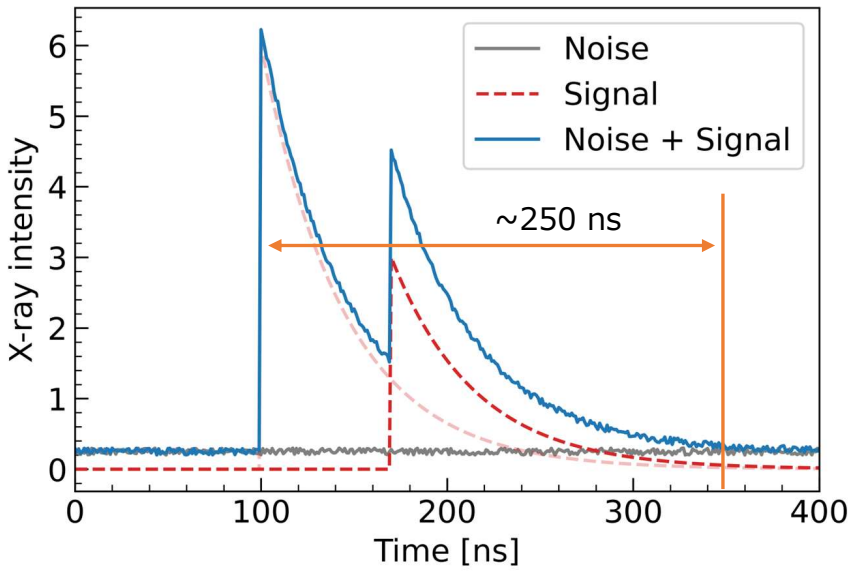

Figure 3.17: Simulated X-ray signals. Since there is a dead time of about 250 ns, X-ray signals arriving during that time are not counted.

shown in Fig. 3.20. These results suggest that the iodine contrast agent was nearly completely eliminated from the kidneys after an X-ray CT scan 2 hours after injection.

These results suggest that approximately 2 hours after the injection of iodine, the body circulation has ended and iodine has finally accumulated in the bladder. These are coherent with the previous clinical facts, so we can say that the CT imaging was performed correctly. On the other hand, since the mouse model excreted urine between the two CT scans, it is possible that the concentration in the bladder 2 hours after injection was lower than the concentration measured 30 minutes after injection. This calls for improved CT imaging protocols and to be performed quickly before urine is excreted.

From here, the accuracy of the estimated iodine concentration was verified by calculating the total mass of iodine injected based on the iodine concentration map. First, the iodine mass corresponding to an individual voxel was obtained by multiplying the estimated iodine concentration of the voxel by its volume. The dimensions of one voxel in the concentration map were assumed to be 1 mm $\times$ 1 mm $\times$ 1 mm. The masses of all iodine voxels in the mouse were then summed. The results showed that at 30 minutes after injection, the total mass of iodine was 46.68 $\pm$ 0.18 mg, and at 2 hours after injection, the total mass was 37.85 $\pm$ 0.16 mg. In addition, after concentration correction by Power-Law (see section 3.3.5 for the reason for introducing the correction), the total mass of each is as follows: 62 $\pm$ 7 mg for 30 minutes after dosing and 52 $\pm$ 6 mg for 2 hours after dosing. Referring to section 3.3.5, the concentration estimation using a static phantom mimicking 2-15 mg/mL iodine contrast agent had an error of about 10%. Thus, the concentrations were considered to be corrected with sufficient accuracy to account for the error in total mass in CT imaging at each time in mice. On the other hand, when compared to the physical amount of 60 mg of iodine injected into the mice (calculated as 300 mgI/mL $\times$ 0.2 mL), the data measured at 30 minutes were consistent within the error margin, but the total mass was estimated $\sim$13% lower in the data measured at 2 hours. This cannot be explained by uncertainty in concentration estimation alone. This discrepancy may be due to the fact that the linear array detector covered only the region from the lower neck to the tail of the mouse model (Fig. 3.20), excluding the area containing the thyroid gland, a known iodine accumulation site. In other words, it is conceivable that iodine may have accumulated in the thyroid gland in the CT scan performed 2 hours later, and that the total mass of iodine injected was underestimated because of the unobserved portion of the iodine mass. Alternatively, as noted above, it is possible that the iodine mass present in the body during the measurement was reduced by urination. To reduce these uncertainties, we mention again that it is essential to review the CT imaging protocol and improve the accuracy of the system by minimizing the measurement time.

3.3.7 Three-dimensional concentration mapping of in vivo

As illustrated in Fig. 3.5, the installed X-ray linear array detector was oriented vertically, and the mouse model was positioned with its head facing upwards. This setup enabled us to capture the entire area from the tail to the lower neck in a single CT scanning utilizing all 64 channels of the detector. Furthermore, iodine concentration maps were produced from the obtained CT images within the all energy bands, as depicted in Fig. 3.20.

The center and right images of Fig. 3.20 display the concentration maps acquired 30 minutes and 2 hours after injection of the iodine contrast agent. At 30 minutes after injection, iodine enhancement was observed in the tail, bladder, and kidneys of the mouse model, but only in the bladder at 2 hours after injection. Notably, iodine emphasis is absent in adipose tissue, soft tissue, or bone.

3.4 Conclusion and future prospects

We developed a new PC-CT system and evaluated its imaging performance with respect to an iodine-mimicking static phantom and an iodine contrast agent in vivo in mice. We employed not

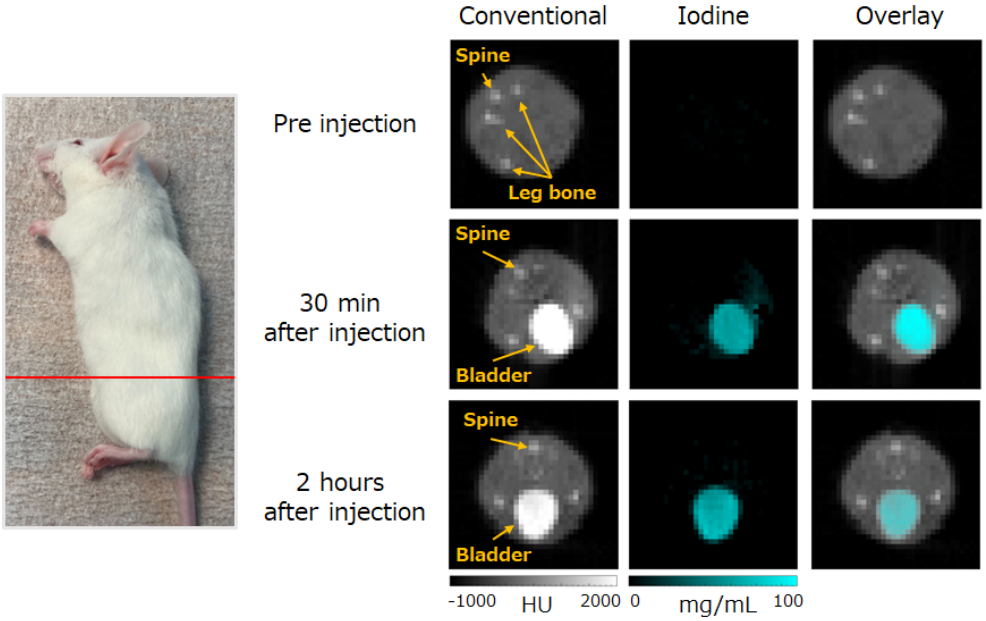

Figure 3.18: Left: Photograph of a mouse model administered anesthesia. Red line marks the cross-sectional slice depicted in the concentration map, corresponding to area of the mouse model abdomen where bladder is located. Right: Conventional-like CT images using X-ray events in the 22–100 keV band, concentration maps, and their overlay images. From top to bottom, in chronological order: before iodine contrast administration, 30 minutes after administration, and 2 hours after administration. It can be seen that iodine accumulates in the bladder after iodine contrast agent injection [47].

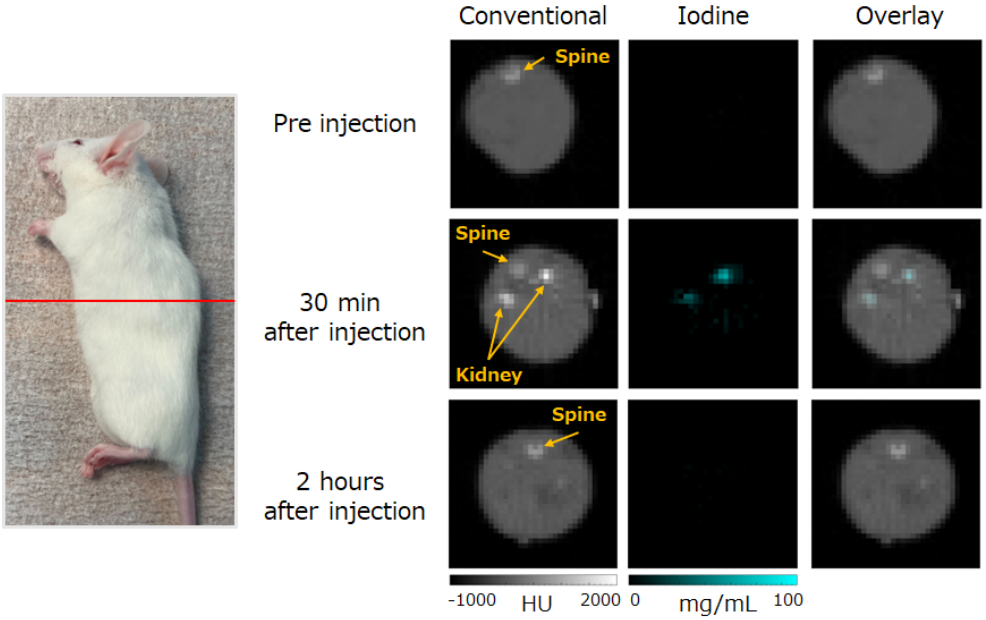

Figure 3.19: Photograph of mouse model and obtained various images. Notations are consistent with Fig. 3.18 except for the red line, which corresponds to area of mouse model chest where kidneys are located [47]. At 30 minutes after administration, there is an accumulation of iodine in the kidney, which disappears after 2 hours.

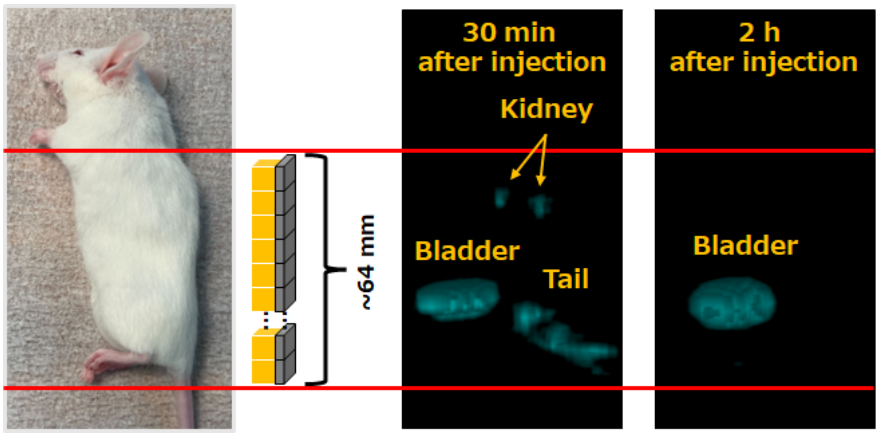

Figure 3.20: Left: Photograph of a mouse model before CT imaging, with the imaging area spanning from the tail to the lower neck, captured using the 64-channel linear array. Center and right: three-dimensional concentration maps observed from the mouse model, taken 30 minutes and 2 hours after injection, respectively [47].

only CT images but also a new technique called concentration mapping to visualize the spatial distribution of iodine.

In a static phantom, the CT values of measured and simulated CT images were evaluated in comparison. The accuracy of concentration estimation was also evaluated, and a simple Power-Law model was used to correct for concentration. This correction model was applied to the following mouse model imaging results.

In the mouse model, CT imaging was performed 30 minutes and 2 hours after tail vein injection of iodine contrast agent, and concentration mapping was performed. The results showed that the concentration map at 30 minutes after showed contrast enhancement in the kidney and bladder, while at 2 hours after, only the bladder showed iodine enhancement. Thus, a temporal change in the spatial distribution of iodine contrast agent in the mouse body was observed. Although the concentration maps facilitated visualization of iodine distribution and concentration, they did not allow visualization of iodine contrast enhancement and concentration in the heart and aorta, the major vascular pathways for iodine. This limitation was mainly due to the rapid blood flow in the heart and aorta and the relatively low temporal resolution of the CT images in this study because the scan time was approximately 25 minutes.

To enhance the time resolution of CT imaging and enable the visualization of contrast agents flowing through the heart and aorta, we plan to upgrade the PC-CT system from its first-generation scanning using a linear array detector system to third-generation scanning using a two-dimensional array detector in the future. This upgrade is expected to reduce the imaging time from approximately 25 minutes with the current system to around 3 minutes, facilitating in vivo dynamic imaging. Additionally, we aim to demonstrate simultaneous in vivo discrimination by injecting multiple contrast agents such as iodine and gadolinium. Such enhancements will establish a new diagnostic system emphasizing different organs with distinct contrast agents.

Chapter 4

Sparse-view CT imaging using photon-counting CT

4.1 Compressed sensing-based image reconstruction algorithm

In the previous chapter 3, imaging of static phantoms and iodine-treated mice was performed using our originally developed photon-counting CT. From this chapter 4, sparse-view image reconstruction is performed using the measurement data obtained in the previous chapter 3.

In X-ray CT, the process of image reconstruction can be conceptualized as solving the linear equation $\mathbf{Ax} = \mathbf{b}$ for $\mathbf{x}$. Here, $\mathbf{x}$ represents the vector of reconstructed images, $\mathbf{A}$ is the system matrix representing the Radon transformation, and $\mathbf{b}$ is the vector of projection data acquired from CT scanning. However, in scenarios where the number of projection data $\mathbf{b}$ is fewer than the size of the reconstructed image $\mathbf{x}$, the problem becomes an underdetermined ill-posed inverse problem, a condition typical in sparse-view CT reconstruction. In such instances, compressive sensing (CS) theory can be applied to reconstruct a cross-sectional image of the subject from sparsely sampled projection data. The sparse-view reconstructed image $\mathbf{x}$ is obtained by minimizing the following cost function $J(\mathbf{x})$:

$$J(\mathbf{x}) = \|\mathbf{Ax} - \mathbf{b}\|_2^2 + \beta\|\mathbf{Wx}\|_1^1\,, \tag{4.1}$$

where the first term represents the loss function, with $\|\cdot\|_2$ denoting the L2-norm, indicating least-squares error. The second term is the regularization term, with $\|\cdot\|_1$ representing the L1-norm. The sparsifying transform $\mathbf{W}$ converts $\mathbf{x}$ into a sparse vector, and the hyperparameter β controls the regularization strength. To achieve the optimal x that minimizes J(x), we used an iterative reconstruction (IR) algorithm based on the majorization-minimization method proposed in our previous study [101, 102]. This is because $J(\mathbf{x})$ cannot be solved analytically because it contains absolute values in the second term, which are not differentiable. This proximity gradient algorithm determines the optimal $\mathbf{x}$ by iteratively minimizing the surrogate function $Q(\mathbf{x};\mathbf{x}^{(k)})$ instead of the cost function $J(\mathbf{x})$. Here, consider the proximity operator to derive the surrogate function $Q(\mathbf{x};\mathbf{x}^{(k)})$. The definition of the proximity operator can be expressed as

$$\mathrm{prox}_\alpha^f(\mathbf{v}) \triangleq \arg\min\left\{ f(\mathbf{x}) + \frac{\alpha}{2}\|\mathbf{x}-\mathbf{v}\|_2^2 \right\} \tag{4.2}$$

where, α denotes the Lipschitz constant and arg min denotes the set of optimal solutions $\mathbf{x}$. Thus, the proximity gradient algorithm follows using the proximity operator.

$$\begin{aligned} \mathrm{prox}_\alpha^{\beta U}(\mathbf{x}^{(k)} - \frac{1}{\alpha}\nabla L(\mathbf{x}^{(k)})) &= \arg\min\left\{ \beta U(\mathbf{x}) + \frac{\alpha}{2}\|\mathbf{x}-\mathbf{x}^{(k)} + \frac{1}{\alpha}\nabla L(\mathbf{x}^{(k)})\|_2^2 \right\} \\ &\sim \frac{\alpha}{2}\|\mathbf{x}-\mathbf{x}^{(k)} + \frac{1}{\alpha}\nabla L(\mathbf{x}^{(k)})\|_2^2 + \beta\|\mathbf{Ix}-\mathbf{Mx}\|_1^1 \\ &\equiv Q(\mathbf{x};\mathbf{x}^{(k)}) \end{aligned} \tag{4.3}$$

where $L(\mathbf{x}) = \|\mathbf{A}\mathbf{x} - \mathbf{b}\|_2^2$, $U(\mathbf{x}) = \|\mathbf{W}\mathbf{x}\|_1^1$. And $\mathbf{M}$ represents a low-pass filter that satisfies $\mathbf{W} = \mathbf{I} - \mathbf{M}$ and $\mathbf{I}$ represents the identity matrix. Here, we again define the surrogate function Q.

$$\begin{aligned} Q(\mathbf{x}; \mathbf{x}^{(k)}) &= \frac{\alpha}{2}\|\mathbf{x} - \mathbf{d}(\mathbf{x}^{(k)})\|_2^2 + \beta \sum_{j=1}^{J} |x_j - \mathbf{M}_j(\mathbf{d}(\mathbf{x}^{(k)}))|\,, \\ \mathbf{d}(\mathbf{x}^{(k)}) &\equiv \mathbf{x}^{(k)} - \frac{1}{\alpha}\nabla L(\mathbf{x}^{(k)}) = \mathbf{x}^{(k)} - \frac{2}{\alpha}\mathbf{A}^{\mathsf{T}}(\mathbf{A}\mathbf{x}^{(k)} - \mathbf{b})\,, \end{aligned} \tag{4.4}$$

where $\mathbf{x}^{(k)}$ and $\mathbf{M}_j(\mathbf{d}(\mathbf{x}^{(k)}))$ denote the image $\mathbf{x}$ of the k-th iteration and the j-th pixel value of $\mathbf{M}\mathbf{d}(\mathbf{x}^{(k)})$, respectively. Furthermore, since $Q(\mathbf{x}; \mathbf{x}^{(k)})$ can be thought of as a translation by $\mathbf{M}_j(\mathbf{d}(\mathbf{x}^{(k)}))$ from the basic form of the proximity operator, the updated image $\mathbf{x}^{(k+1)}$ can be expressed as follows:

$$\mathbf{x}_j^{(k+1)} = \begin{cases} \mathbf{d}_j(\mathbf{x}^{(k)}) - \dfrac{\beta}{\alpha}, & \mathbf{d}_j(\mathbf{x}^{(k)}) - \mathbf{M}_j(\mathbf{d}(\mathbf{x}^{(k)})) > \dfrac{\beta}{\alpha}, \\ \mathbf{d}_j(\mathbf{x}^{(k)}) + \dfrac{\beta}{\alpha}, & \mathbf{d}_j(\mathbf{x}^{(k)}) - \mathbf{M}_j(\mathbf{d}(\mathbf{x}^{(k)})) < -\dfrac{\beta}{\alpha}, \\ \mathbf{M}_j(\mathbf{d}(\mathbf{x}^{(k)}))\,, & \text{otherwise}, \end{cases} \tag{4.5}$$

Here, $\mathbf{d}_j(\mathbf{x}^{(k)})$ represents the j-th pixel value of $\mathbf{d}(\mathbf{x}^{(k)})$. In this experiment, the filter $\mathbf{M}$ was applied as total variation (TV) as it was the first application of the sparse-view CT algorithm to PC-CT images:

$$\mathbf{M}(\mathbf{d}(\mathbf{x}^{(k)})) \equiv \mathbf{d}(\mathbf{x}^{(k)}) - \frac{2}{\alpha}\nabla\mathbf{TV}(\mathbf{x}^{(k)}) \tag{4.6}$$

Here, $\nabla\mathbf{TV}(\mathbf{x}^{(k)})$ denotes the TV-norm differential, including an infinitesimal quantity $\varepsilon = 1.0 \times 10^{-4}$, and α is fixed at 1000.

With the above, $\mathbf{M}_j(\mathbf{d}(\mathbf{x}^{(k)}))$ and $\mathbf{d}_j(\mathbf{x}^{(k)})$ are calculated at the update timing of the image, and $\mathbf{x}_j^{(k+1)}$ is iteratively updated according to the conditions. The end timing of updating was set to be when the difference between the reconstructed image using the full projection and $\mathbf{x}_j^{(k+1)}$ becomes sufficiently small (0.000001). In the next section, the image analysis procedure is described.

4.2 Image analysis procedures

In this study, the amount of projection data that could be downsampled while maintaining image quality was investigated according to the following procedure. This involved several steps:

1. Determination of Hyperparameter β using Structural Similarity (SSIM) [103]:
   - Application of the IR-based algorithm to the measured real projection data without downsampling.
   - Sweeping β from 10^{-4} to 10^{1} by one digit, generating CT images (referred to as IR-based CT images).
   - Comparison of the image quality of IR-based CT images at different β values with that of CT images reconstructed by FBP for each energy band using the SSIM index.
2. Application of Sparse-view Image-Reconstruction Algorithm to Downsampled Projection Data:
   - Downsampling of real projection data at regular intervals to simulate a sparse-view situation.
   - Downsampling ratios for the rod phantoms were 1/2, 1/4, 1/5, 1/8, 1/10, and 1/20. That is, 100, 50, 40, 25, 20, and 10 projections. For the mouse model, downsampling ratios were 1/2, 1/4, 1/6, and 1/8 (24, 12, 8, and 6 projections, respectively).

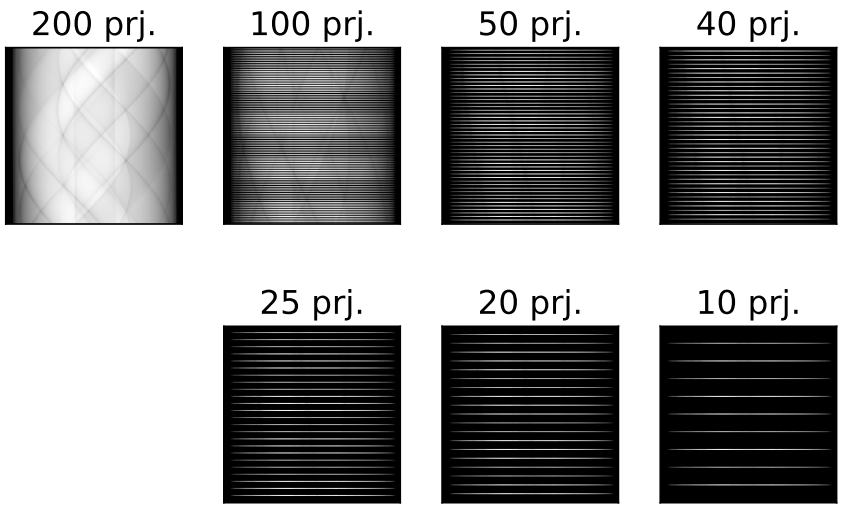

Figure 4.1: Sinograms of CT imaging of static phantoms at various projection numbers. The number of projections were thinned to be equally spaced.

- Application of the sparse-view reconstruction algorithm to the downsampled projection data to obtain sparse-view CT images with β fixed at the value determined previously.

3. Evaluation of Image Quality using SSIM:

- Evaluation of image quality using the SSIM index to determine the lower limit of the downsampling ratio at which the image quality remains acceptable.
- Concentration maps are also evaluated with various downsampling ratio.

This comprehensive procedure allowed for the determination of an optimal downsampling ratio while ensuring acceptable image quality, facilitating more efficient data acquisition and reconstruction in sparse-view CT imaging scenarios. Here is a supplemental explanation of procedure (1). In general, cross-validation is used to determine the hyperparameter β in the analysis of sparse images. However, this requires a huge amount of observational data to implement, which is impractical in this study. Therefore, β selection was conducted according to the procedure shown above. The index SSIM used in the β selection and the evaluation of image quality is defined as follows:

$$SSIM = \frac{(2\mu_x\mu_y + C_1)(2\sigma_{xy} + C_2)}{(\mu_x^2 + \mu_y^2 + C_1)((\sigma_x^2 + \sigma_y^2 + C_2)}, \tag{4.7}$$

where μ and σ denote the mean value of the reconstructed image and standard deviation, respectively. $C1$ (= 0.01) and $C2$ (= 0.03) are constants introduced to avoid unstable SSIM indices when the denominator approaches zero. SSIM takes values from 0 to 1, with higher values indicating greater similarity between the two images. In this study, SSIM of 0.9 or higher is considered to be one of the criteria for judgment.

In this study, the iterative sparse-view reconstruction process was executed until convergence, ensuring the stability and accuracy of the reconstructed CT images. For the static phantoms, the computation time for iterative reconstruction up to 3000 iterations varied depending on the number of projections, ranging from a minimum of 20 seconds for 10 projections to a maximum of 210 seconds for 200 projections. Conversely, for the mouse model, the computation time remained consistently low, taking less than 1 second for any number of projections up to 500 iterations. This efficient computational performance highlights the feasibility of applying sparse-view reconstruction techniques in practical CT imaging scenarios, even for complex subjects such as small animals.

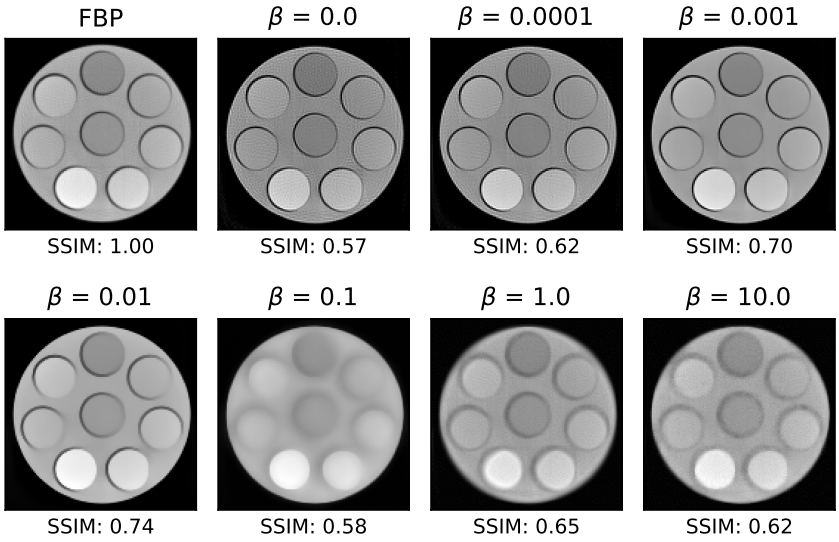

Figure 4.2: FBP-based and IR-based CT image of the static phantom with 200 projections in the 11.2–33.2 keV band. The β is varied and the image quality is evaluated by SSIM.

4.3 Results of static phantom imaging

4.3.1 β selsction

In the left panel of Fig. 4.2, the results for the IR-based CT images are depicted, applying the IR-based method within the energy band of 11.2–33.2 keV without downsampling the number of projections (i.e., utilizing 200 projections). To determine the optimal hyperparameter β, the Structural Similarity Index (SSIM) between the Filtered Back Projection (FBP)-based and IR-based CT images was computed for each β value. Notably, $\beta = 0.01$ yielded the highest SSIM, as indicated in the right panel of Fig. 4.3. This suggests that the image characteristics at $\beta = 0.01$ closely resemble those of the FBP-based CT image, indicating minimal degradation despite the lack of downsampling in projection numbers.

Similar evaluations were conducted for CT images in other energy bands (i.e., 33.2–55.2, 55.2–65.0, 65.0, 75.0, 75.0–90.0, 90.0–120.0 keV), consistently yielding the highest SSIMs at $\beta = 0.01$. Thus, β was fixed at this value for all energy bands. However, it's worth noting that the SSIMs obtained with $\beta = 0.01$ (ranging from 0.63 to 0.75 for each energy band) may not be sufficiently high to discern visual differences, as an SSIM $\gtrsim 0.90$ is typically required to perceive images as identical.

The lower SSIM indices could be attributed to the noise component in the projection data, stemming from statistical fluctuations in X-ray photons. IR algorithms tend to mitigate noise and smoothen images, resulting in reduced noise in IR-based CT images compared to FBP-based ones. Consequently, the presence of image noise, leading to lower SSIM indices, is more prominent in FBP-based CT images. These observations underscore the importance of considering such noise effects when estimating the optimal β value.

4.3.2 Downsampling of projections

In Fig. 4.5, the results of sparse-view image reconstruction with different downsampling ratios are presented. The sparse-view CT images and corresponding Structural Similarity Index (SSIM) values in the energy band of 11.2–33.2 keV are illustrated. Each SSIM value was computed by comparing the CT images reconstructed with and without downsampling, both at $\beta = 0.01$. Similar SSIM values for other energy bands were also obtained and are summarized in Fig. 4.6.

As depicted in Fig. 4.6, the SSIM indices between CT images without downsampling and those

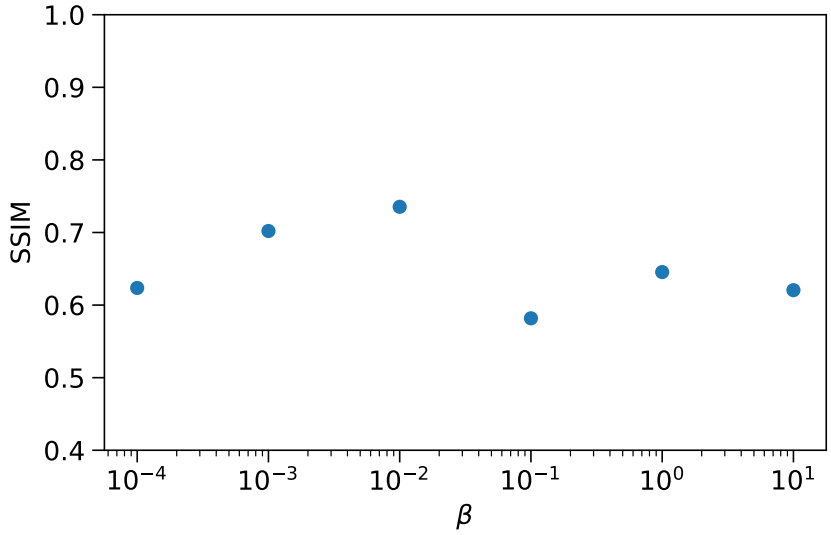

Figure 4.3: SSIM obtained from IR-based CT images when FBP-based is used as the reference. the best SSIM was obtained at β=0.01.

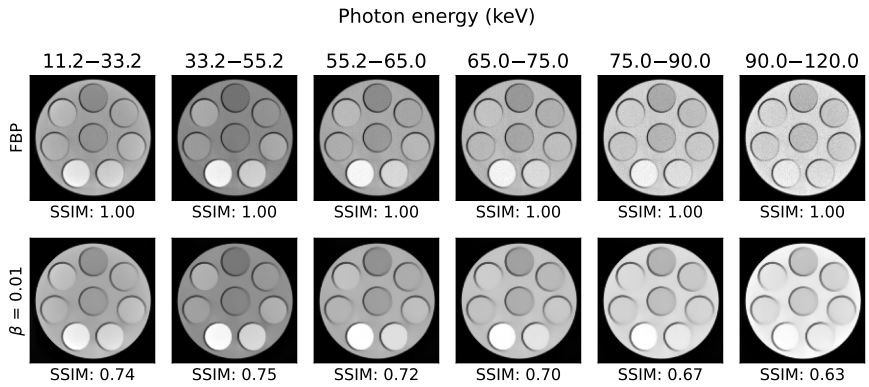

Figure 4.4: FBP-baed and IR-based CT images reconstructed from 200 projections of the phantoms for each energy band. IR-based is shown when beta = 0.01, chosen in the beta selection.

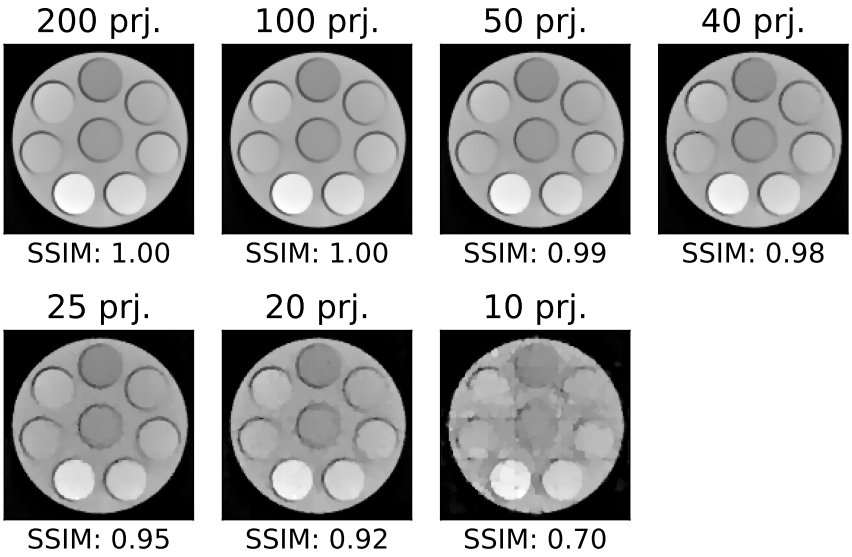

Figure 4.5: Sparse-view CT images of static phantoms from 11.2 to 33.2 keV. Various downsampling ratios are shown, with SSIM based on 200 projections; at 10 projections, there is clear image degradation.

with downsampling ratios of 1/10 or higher (i.e., 20, 25, 40, 50, and 100 projections) exceeded ∼0.90 for the rod phantoms.

4.3.3 Concentration mapping

The iodine concentration maps were also computed, as depicted in Fig. 4.7. For detailed information on the concentration estimation method, please refer to the literature [47]. The SSIM values of the concentration maps were consistently $\gtrsim$0.90 for downsampling ratios of 1/10 or higher. Moreover, the estimated iodine concentrations remained consistent with those obtained without downsampling, as illustrated in Fig. 4.8. Therefore, a downsampling ratio of 1/10 (i.e., 20 projections) was deemed an acceptable lower limit in this experiment. This implies that image quality was preserved even with a tenfold reduction in the number of projections compared to the original setting. Consequently, reducing both imaging time and exposure dose to 1/10 is feasible.

4.4 Results of mouse model imaging

4.4.1 Downsampling of projections

As with the static phantom, image analysis of the mouse model was evaluated by SSIM for image quality after selecting β according to the procedure outlined in Section 4.2. Interestingly, the largest SSIM (i.e., the most similarity to FBP-based CT images) was obtained when β was 0.001, which was different from the rod phantom ($\beta = 0.01$). One possible factor is the complexity of the subject's structure. Since the mouse model is a living organism, its internal structure is complex, while the static phantom has a relatively simple structure. In addition, beta is a parameter that adjusts the smoothness of the updated image when reconstructing CT images, and the smaller the beta is, the more easily the original structure is preserved. In other words, in the mouse model, if beta is made too large, the in vivo structure is lost. Therefore, it can be assumed that the similarity in image quality between the FBP-based CT image and the sparse-view image increases when the beta is smaller than that of the static phantom. Each sparse-view CT image of the mouse abdomen was obtained by sparse-view reconstruction of the down-sampled (24, 12, 8, 6 projections) projection data with β fixed at 0.001 (Fig. 4.9). Subsequently, we calculated the SSIMs without downsampling and with varying downsampling ratios for each energy band, as depicted in Fig. 4.9. Remarkably,

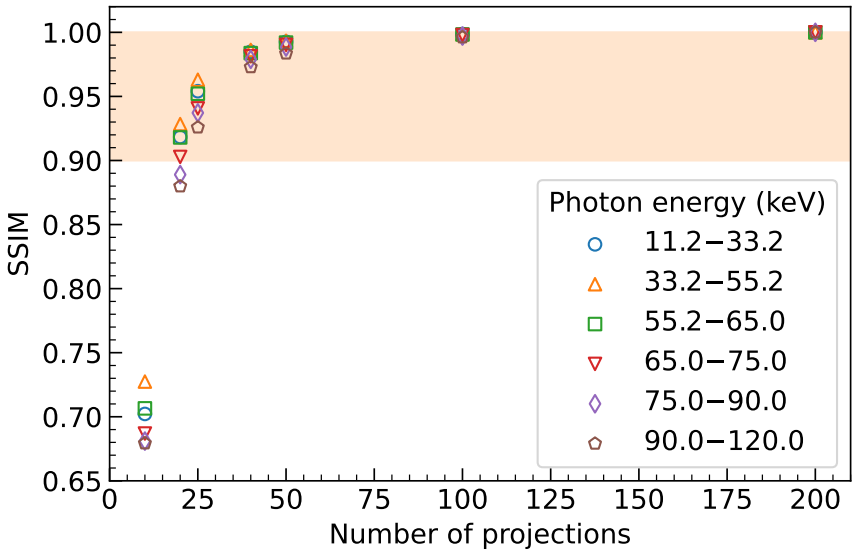

Figure 4.6: Relationship between the SSIM and the number of projections in all energy bands. The orange shaded area represents $0.9 \leq SSIM \leq 1.0$, which generally means that image quality is preserved in this range.

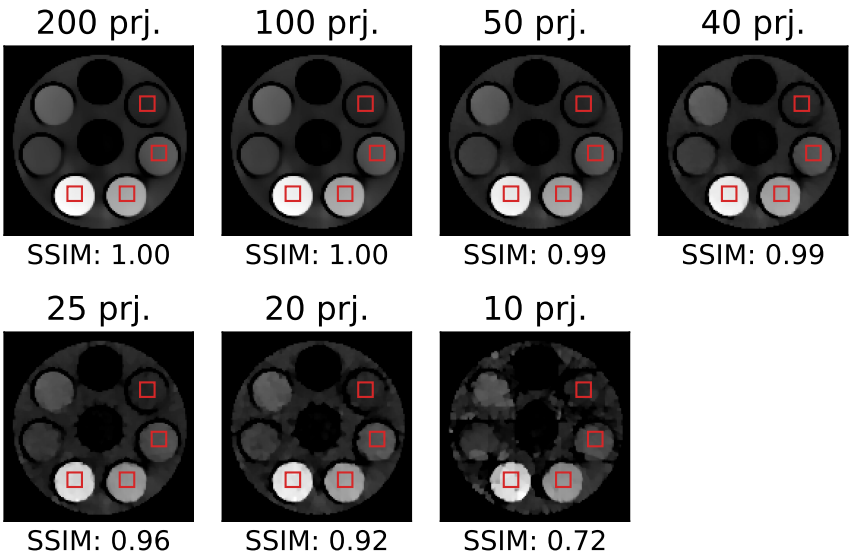

Figure 4.7: Iodine concentration maps for various downsampling ratios. Also shown are SSIMs based on 200 projections as well as CT images. The mean and standard deviation of each iodine concentration in the red box was used for analysis.

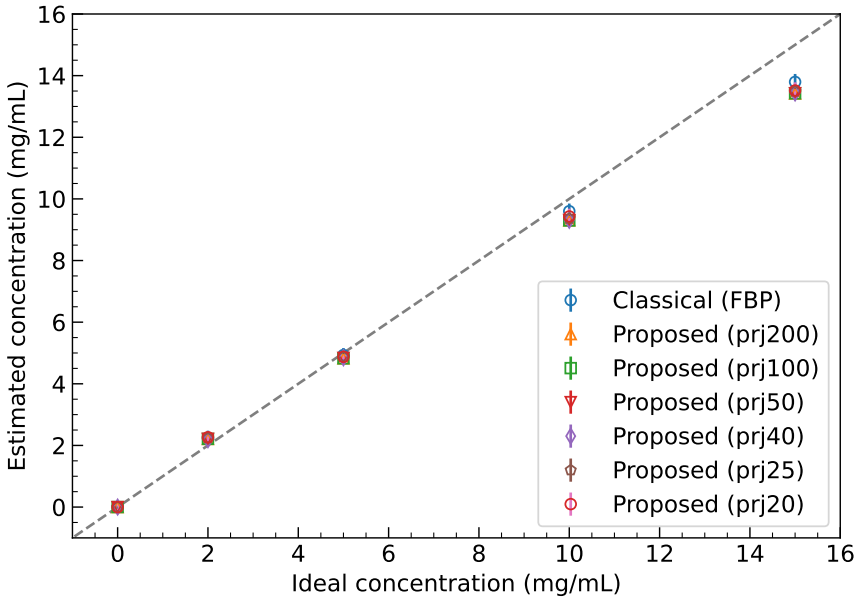

Figure 4.8: Estimated iodine concentrations in each projection compared to ideal concentrations. The mean and standard deviation of the iodine concentration were obtained from the red square box in each concentration map shown in the Fig. 4.7. The FBP results for the 200 projection are also shown, and a comparison of these results shows that they are consistent.

the SSIMs of the CT images across all energy bands were consistently $\gtrsim$0.90 with 12 projections or more, as demonstrated in Fig. 4.10. Additionally, the SSIM of the iodine concentration map with 24 projections exceeded $\gtrsim$0.90 (Fig. 4.11). As a result, the mouse model used in this experiment has the potential to shorten the imaging time and reduce the radiation dose without compromising image quality up to 24 projections (i.e., up to 1/2 of the original number of projections). Notably, the mouse model's more complex structure and smaller number of image pixels likely contributed to differences in downsampling ratios compared to the rod phantoms.

4.5 Conclusion and future prospects

In this study, downsampling was performed on the projection data acquired by our originally developed SiPM-based PC-CT system. A sparse-view reconstruction algorithm based on TV minimization was applied to the sparse-sampled projection data, and the image quality of the resulting sparse-view CT images was evaluated.

As in Chapter 3, a static rod phantom and a mouse model injected with iodine contrast agent were used as subjects. The results showed that image quality was maintained even when the number of projections was reduced by a factor of up to 10 for the static phantom and by a factor of up to 2 for the mouse model. Thus, the sparse-view reconstruction algorithm used in this study was effective for real projection data obtained from SiPM-based PC-CT and showed great potential for reducing imaging time and radiation dose.

However, the first-generation linear array of SiPM-based detectors used in the study resulted in considerably longer imaging times compared to current clinical CT systems, which typically use third-generation technology. To address this challenge, efforts are underway to develop a two-dimensional array of SiPM detectors. Additionally, plans include reducing the pixel size of the detector to enhance spatial resolution from the current 1×1 mm^2/pixel to 0.5×0.5 mm^2/pixel. Future work will report the results of the CS-based image-reconstruction algorithm using the newly developed two-dimensional detector system. Moreover, comparisons will be made with CdTe and CdZnTe detectors to assess the clinical feasibility of SiPM detectors.

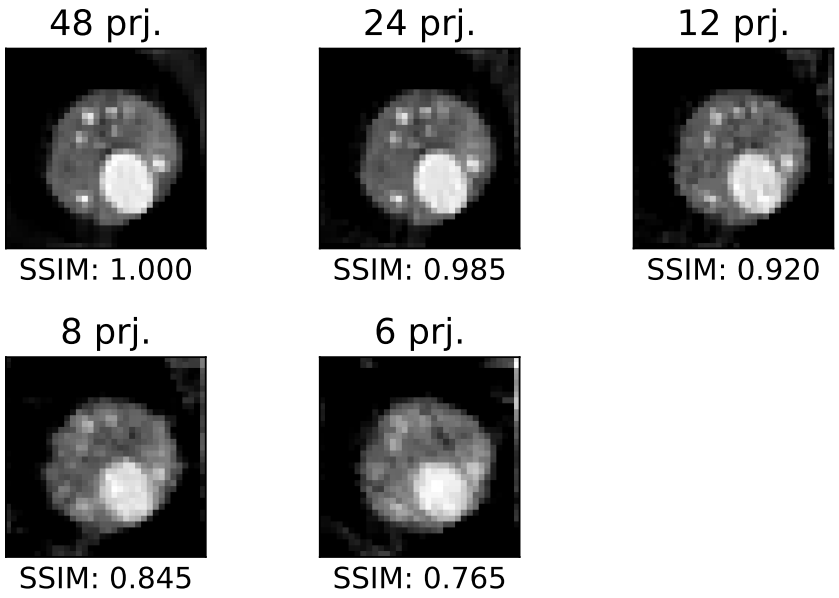

Figure 4.9: Sparse-view CT images of mouse abdomen reconstructed at various downsampling ratios (23.2–33.2 keV). SSIM is based on 48 projections; below 8 projections it cannot be reconstructed well and the abdominal structure appears to be collapsed.

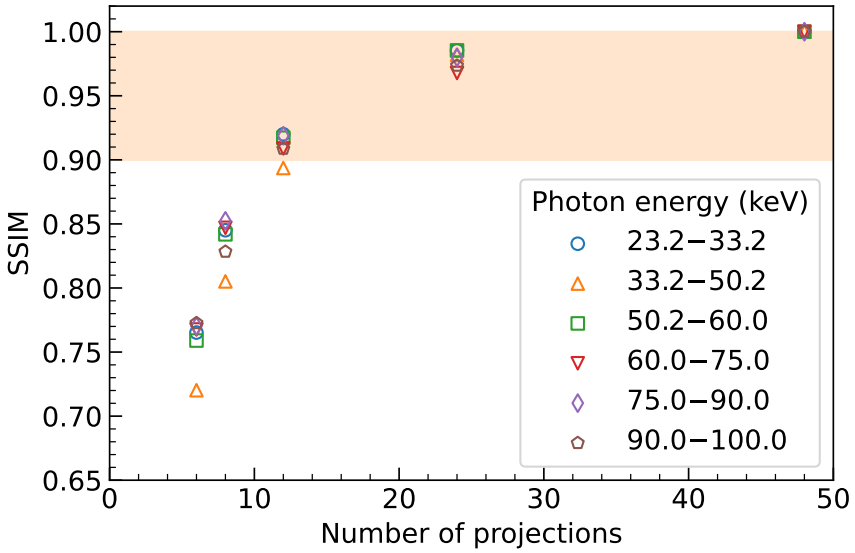

Figure 4.10: Relationship between SSIM and projection in all energy bands of the mouse model. The orange shaded area represents $0.9 \leq SSIM \leq 1.0$. The image quality degradation decays more rapidly than static phantoms.

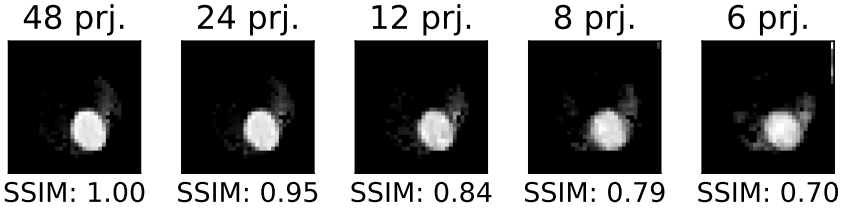

Figure 4.11: Iodine concentration maps of mouse abdomen at various downsampling ratios; as with CT images, SSIM is based on 48 projections.

Chapter 5

Conclusion and future prospects

5.1 Photon-counting CT

The study introduced a novel PC-CT system and explored its effectiveness in imaging iodine contrast agents using K-edge imaging and concentration mapping techniques. While successful in revealing temporal changes in iodine distribution within certain organs like the kidneys and bladder, these methods faced challenges in visualizing iodine within the heart or aorta due to rapid blood flow and limited time resolution. To address this, the researchers proposed upgrading to a third-generation PC-CT system for faster imaging, enabling real-time visualization of contrast agents. Moreover, they aim to demonstrate the system's capability for simultaneous imaging with multiple contrast agents, which could revolutionize diagnostic imaging by emphasizing organ-specific contrasts.

5.2 Sparse-view CT

Additionally, the study developed and applied a sparse-view reconstruction algorithm to sparsely sampled projection data obtained from a SiPM-based PC-CT system. Using static rod phantoms and a mouse model injected with an iodine contrast agent, the researchers found that image quality remained high even with a significant reduction in the number of projections. This suggests that the sparse-view reconstruction algorithm holds promise for achieving shorter imaging times and reduced radiation doses, particularly in SiPM-based PC-CT systems. Overall, these findings offer valuable insights into advancing CT imaging technology for more efficient and effective diagnostic procedures.

Bibliography

[1] G. N. Hounsfield. Computerized transverse axial scanning (tomography): Part 1. Description of system. *British Journal of Radiology*, 46(552):1016–1022, 01 2014.

[2] James Ambrose. Computerized transverse axial scanning (tomography): Part 2. Clinical application*. *British Journal of Radiology*, 46(552):1023–1047, 01 2014.

[3] B. J. Perry and C. Bridges. Computerized transverse axial scanning (tomography): Part 3. Radiation dose considerations. *British Journal of Radiology*, 46(552):1048–1051, 01 2014.

[4] Akinori Hata, Masahiro Yanagawa, Osamu Honda, Noriko Kikuchi, Tomo Miyata, Shinsuke Tsukagoshi, Ayumi Uranishi, and Noriyuki Tomiyama. Effect of matrix size on the image quality of ultra-high-resolution ct of the lung: Comparison of 512 × 512, 1024 × 1024, and 2048 × 2048. *Academic Radiology*, 25(7):869–876, 2018.

[5] Hrvoje Lusic and Mark W. Grinstaff. X-ray-computed tomography contrast agents. *Chemical Reviews*, 113(3):1641–1666, 2013. PMID: 23210836.

[6] Kyongtae T. Bae. Intravenous contrast medium administration and scan timing at ct: Considerations and approaches. *Radiology*, 256(1):32–61, 2010. PMID: 20574084.

[7] Judith Kooiman, Sharif M. Pasha, Wendy Zondag, Yvo W.J. Sijpkens, Aart J. van der Molen, Menno V. Huisman, and Olaf M. Dekkers. Meta-analysis: Serum creatinine changes following contrast enhanced ct imaging. *European Journal of Radiology*, 81(10):2554–2561, 2012.

[8] Japan Ministry of the environment. Comparison of exposure doses per year, 2008. `https://www.env.go.jp/chemi/rhm/h29kisoshiryo/h29kiso-02-05-03.html`.

[9] OECD. Oecd health statistics 2019, 2019. `https://www.oecd.org/health/OECD-Health-Statistics-2019-Frequently-Requested-Data.xls`.

[10] R. E. Alvarez and A. Macovski. Energy-selective reconstructions in x-ray computerised tomography. *Physics in Medicine & Biology*, 21(5):733, sep 1976.

[11] Bernhard Krauss, Katharine L. Grant, Bernhard T. Schmidt, and Thomas G. Flohr. The importance of spectral separation: An assessment of dual-energy spectral separation for quantitative ability and dose efficiency. *Investigative Radiology*, 50(2):114–118, 2015.

[12] R Gutjahr, AF Halaweish, Z Yu, S Leng, L Yu, Z Li, SM Jorgensen, EL Ritman, S Kappler, and CH McCollough. Human imaging with photon counting-based computed tomography at clinical dose levels: Contrast-to-noise ratio and cadaver studies. *Investigative Radiology*, 51(7):421–429, jul 2016.

[13] Mats Persson, Ben Huber, Staffan Karlsson, Xuejin Liu, Han Chen, Cheng Xu, Moa Yveborg, Hans Bornefalk, and Mats Danielsson. Energy-resolved ct imaging with a photon-counting silicon-strip detector. *Physics in Medicine & Biology*, 59(22):6709, oct 2014.

[14] Katsuyuki Taguchi and Jan S. Iwanczyk. Vision 20/20: Single photon counting x-ray detectors in medical imaging. *Medical Physics*, 40(10):100901, 2013.

[15] Hans Bornefalk and Mats Danielsson. Photon-counting spectral computed tomography using silicon strip detectors: a feasibility study. *Physics in Medicine & Biology*, 55(7):1999, mar 2010.

[16] Cheng Xu, Mats Danielsson, and Hans Bornefalk. Evaluation of energy loss and charge sharing in cadmium telluride detectors for photon-counting computed tomography. *IEEE Transactions on Nuclear Science*, 58(3):614–625, 2011.

[17] Polad M Shikhaliev, Shannon G Fritz, and John W Chapman. Photon counting multienergy x-ray imaging: Effect of the characteristic x rays on detector performance. *Medical physics*, 36(11):5107–5119, 2009.

[18] Thilo Michel, Gisela Anton, M Böhnel, J Durst, M Firsching, A Korn, B Kreisler, A Loehr, F Nachtrab, D Niederlöhner, et al. A fundamental method to determine the signal-to-noise ratio (snr) and detective quantum efficiency (dqe) for a photon counting pixel detector. *Nuclear Instruments and Methods in Physics Research Section A: Accelerators, Spectrometers, Detectors and Associated Equipment*, 568(2):799–802, 2006.

[19] J Xu, W Zbijewski, G Gang, JW Stayman, K Taguchi, M Lundqvist, E Fredenberg, John Anthony Carrino, and JH Siewerdsen. Cascaded systems analysis of photon counting detectors. *Medical physics*, 41(10):101907, 2014.

[20] Ewald Roessl, Bernhard Brendel, Klaus-Juergen Engel, Jens-Peter Schlomka, Axel Thran, and Roland Proksa. Sensitivity of photon-counting based k-edge imaging in x-ray computed tomography. *IEEE transactions on medical imaging*, 30(9):1678–1690, 2011.

[21] Robert E Alvarez. Signal to noise ratio of energy selective x-ray photon counting systems with pileup. *Medical physics*, 41(11):111909, 2014.

[22] Katsuyuki Taguchi, Mengxi Zhang, Eric C Frey, Xiaolan Wang, Jan S Iwanczyk, Einar Nygard, Neal E Hartsough, Benjamin MW Tsui, and William C Barber. Modeling the performance of a photon counting x-ray detector for ct: Energy response and pulse pileup effects. *Medical physics*, 38(2):1089–1102, 2011.

[23] Adam S Wang, Daniel Harrison, Vladimir Lobastov, and J Eric Tkaczyk. Pulse pileup statistics for energy discriminating photon counting x-ray detectors. *Medical physics*, 38(7):4265–4275, 2011.

[24] Glenn F Knoll. *Radiation detection and measurement*. John Wiley & Sons, 2010.

[25] Polad M Shikhaliev. Beam hardening artefacts in computed tomography with photon counting, charge integrating and energy weighting detectors: a simulation study. *Physics in Medicine & Biology*, 50(24):5813, 2005.

[26] A Pourmorteza, R Symons, DS Reich, M Bagheri, TE Cork, S Kappler, S Ulzheimer, and DA Bluemke. Photon-counting ct of the brain: in vivo human results and image-quality assessment. *American Journal of Neuroradiology*, 38(12):2257–2263, 2017.

[27] Rolf Symons, Daniel S Reich, Mohammadhadi Bagheri, Tyler E Cork, Bernhard Krauss, Stefan Ulzheimer, Steffen Kappler, David A Bluemke, and Amir Pourmorteza. Photon-counting ct for vascular imaging of the head and neck: first in vivo human results. *Investigative radiology*, 53(3):135, 2018.

[28] Rolf Symons, Amir Pourmorteza, Veit Sandfort, Mark A Ahlman, Tracy Cropper, Marissa Mallek, Steffen Kappler, Stefan Ulzheimer, Mahadevappa Mahesh, Elizabeth C Jones, et al. Feasibility of dose-reduced chest ct with photon-counting detectors: initial results in humans. *Radiology*, 285(3):980–989, 2017.

[29] Daniela Muenzel, Daniel Bar-Ness, Ewald Roessl, Ira Blevis, Matthias Bartels, Alexander A. Fingerle, Stefan Ruschke, Philippe Coulon, Heiner Daerr, Felix K. Kopp, Bernhard Brendel, Axel Thran, Michal Rokni, Julia Herzen, Loic Boussel, Franz Pfeiffer, Roland Proksa, Ernst J. Rummeny, Philippe Douek, and Peter B. Noël. Spectral photon-counting ct: Initial experience with dual–contrast agent k-edge colonography. *Radiology*, 283(3):723–728, 2017. PMID: 27918709.

[30] J P Schlomka, E Roessl, R Dorscheid, S Dill, G Martens, T Istel, C Bäumer, C Herrmann, R Steadman, G Zeitler, A Livne, and R Proksa. Experimental feasibility of multi-energy photon-counting k-edge imaging in pre-clinical computed tomography. *Physics in Medicine & Biology*, 53(15):4031, jul 2008.

[31] Shuai Leng, Zhicong Yu, Ahmed Halaweish, Steffen Kappler, Katharina Hahn, Andre Henning, Zhoubo Li, John Lane, David L. Levin, Steven Jorgensen, Erik Ritman, and Cynthia McCollough. Dose-efficient ultrahigh-resolution scan mode using a photon counting detector computed tomography system. *Journal of Medical Imaging*, 3(4):043504, 2016.

[32] Polad M Shikhaliev. Computed tomography with energy-resolved detection: a feasibility study. *Physics in Medicine & Biology*, 53(5):1475, feb 2008.

[33] Ann-Christin Rößler, Willi Kalender, Daniel Kolditz, Christian Steiding, Veikko Ruth, Caroline Preuss, Sandra Christina Peter, Barbara Brehm, Matthias Hammon, Rüdiger Schulz-Wendtland, and Evelyn Wenkel. Performance of photon-counting breast computed tomography, digital mammography, and digital breast tomosynthesis in evaluating breast specimens. *Academic Radiology*, 24(2):184–190, 2017.

[34] Amir Pourmorteza, Rolf Symons, Veit Sandfort, Marissa Mallek, Matthew K. Fuld, Gregory Henderson, Elizabeth C. Jones, Ashkan A. Malayeri, Les R. Folio, and David A. Bluemke. Abdominal imaging with contrast-enhanced photon-counting ct: First human experience. *Radiology*, 279(1):239–245, 2016. PMID: 26840654.

[35] Kishore Rajendran, Martin Petersilka, André Henning, Elisabeth R. Shanblatt, Bernhard Schmidt, Thomas G. Flohr, Andrea Ferrero, Francis Baffour, Felix E. Diehn, Lifeng Yu, Prabhakar Rajiah, Joel G. Fletcher, Shuai Leng, and Cynthia H. McCollough. First clinical photon-counting detector ct system: Technical evaluation. *Radiology*, 303(1):130–138, 2022. PMID: 34904876.

[36] T. Takahashi and S. Watanabe. Recent progress in cdte and cdznte detectors. *IEEE Transactions on Nuclear Science*, 48(4):950–959, 2001.

[37] Roger Steadman et al. Chromaix: Fast photon-counting asic for spectral computed tomography. *Nuclear Instruments and Methods in Physics Research Section A*, 648:S211–S215, 2011.

[38] Roger Steadman et al. Chromaix2: A large area, high count-rate energy-resolving photon counting asic for a spectral ct prototype. *Nuclear Instruments and Methods in Physics Research Section A*, 862:18–24, 2017.

[39] Csaba Szeles, Stephen A. Soldner, Steve Vydrin, Jesse Graves, and Derek S. Bale. Cdznte semiconductor detectors for spectroscopic x-ray imaging. *IEEE Transactions on Nuclear Science*, 55(1):572–582, 2008.

[40] W.C. Barber, J.C. Wessel, E. Nygard, and J.S. Iwanczyk. Energy dispersive cdte and cdznte detectors for spectral clinical ct and ndt applications. *Nuclear Instruments and Methods in Physics Research Section A: Accelerators, Spectrometers, Detectors and Associated Equipment*, 784:531–537, 2015. Symposium on Radiation Measurements and Applications 2014 (SORMA XV).

[41] Thomas Sartoretti, Joachim E Wildberger, Thomas Flohr, and Hatem Alkadhi. Photon-counting detector ct: early clinical experience review. *The British Journal of Radiology*, 96(1147):20220544, 2023. PMID: 36633005.

[42] Francis I. Baffour, Katrina N. Glazebrook, Andrea Ferrero, Shuai Leng, Cynthia H. McCollough, Joel G. Fletcher, and Kishore Rajendran. Photon-counting detector ct for musculoskeletal imaging: A clinical perspective. *American Journal of Roentgenology*, 220(4):551–560, 2023. PMID: 36259593.

[43] H. Morita et al. Novel photon-counting low-dose computed tomography using a multi-pixel photon counter. *Nuclear Instruments and Methods in Physics Research Section A*, 857:58–65, 2017.

[44] T. Maruhashi et al. Evaluation of a novel photon-counting ct system using a 16-channel mppc array for multicolor 3-d imaging. *Nuclear Instruments and Methods in Physics Research Section A*, 936:5–9, 2019.

[45] T. Maruhashi et al. Demonstration of multiple contrast agent imaging for the next generation color x-ray ct. *Nuclear Instruments and Methods in Physics Research Section A*, 958:162801, 2020.

[46] H. Kiji et al. 64-channel photon-counting computed tomography using a new mppc-ct system. *Nuclear Instruments and Methods in Physics Research Section A*, 984:164610, 2020.

[47] D. Sato et al. Initial results of in vivo ct imaging of contrast agents using mppc-based photon-counting ct. *Nuclear Instruments and Methods in Physics Research Section A*, 1048:167960, 2023.

[48] Kennan T Smith, Donald C Solmon, and Sheldon L Wagner. Practical and mathematical aspects of the problem of reconstructing objects from radiographs. 1977.

[49] Alfred K Louis and W Törnig. Ghosts in tomography-the null space of the radon transform. *Mathematical Methods in the Applied Sciences*, 3(1):1–10, 1981.

[50] Jorge Llacer. Theory of imaging with a very limited number of projections. *IEEE Transactions on Nuclear Science*, 26(1):596–602, 1979.

[51] S Siltanen, V Kolehmainen, S Järvenpää, J P Kaipio, P Koistinen, M Lassas, J Pirttilä, and E Somersalo. Statistical inversion for medical x-ray tomography with few radiographs: I. general theory. *Physics in Medicine & Biology*, 48(10):1437, may 2003.

[52] Rangaraj Rangayyan, Atam Prakash Dhawan, and Richard Gordon. Algorithms for limited-view computed tomography: an annotated bibliography and a challenge. *Applied optics*, 24(23):4000–4012, 1985.

[53] Leonid I Rudin, Stanley Osher, and Emad Fatemi. Nonlinear total variation based noise removal algorithms. *Physica D: nonlinear phenomena*, 60(1-4):259–268, 1992.

[54] Jean-Luc Starck, Fionn Murtagh, and Jalal M Fadili. *Sparse image and signal processing: wavelets, curvelets, morphological diversity*. Cambridge university press, 2010.

[55] Michael Elad. *Sparse and redundant representations: from theory to applications in signal and image processing*, volume 2. Springer, 2010.

[56] Patrick L. Combettes and Jean-Christophe Pesquet. Proximal splitting methods in signal processing, 2010.

[57] Ingrid Daubechies, Michel Defrise, and Christine De Mol. An iterative thresholding algorithm for linear inverse problems with a sparsity constraint. *Communications on Pure and Applied Mathematics: A Journal Issued by the Courant Institute of Mathematical Sciences*, 57(11):1413–1457, 2004.

[58] Kenneth Lange. *Optimization*, volume 95. Springer Science & Business Media, 2013.

[59] Kenneth Lange, David R Hunter, and Ilsoon Yang. Optimization transfer using surrogate objective functions. *Journal of computational and graphical statistics*, 9(1):1–20, 2000.

[60] Meihua Li, Haiquan Yang, and Hiroyuki Kudo. An accurate iterative reconstruction algorithm for sparse objects: application to 3d blood vessel reconstruction from a limited number of projections. *Physics in Medicine & Biology*, 47(15):2599, 2002.

[61] Emil Y Sidky, Chien-Min Kao, and Xiaochuan Pan. Accurate image reconstruction from few-views and limited-angle data in divergent-beam ct. *Journal of X-ray Science and Technology*, 14(2):119–139, 2006.

[62] Emil Y Sidky and Xiaochuan Pan. Image reconstruction in circular cone-beam computed tomography by constrained, total-variation minimization. *Physics in Medicine & Biology*, 53(17):4777, 2008.

[63] Jiayu Song, Qing H Liu, G Allan Johnson, and Cristian T Badea. Sparseness prior based iterative image reconstruction for retrospectively gated cardiac micro-ct. *Medical physics*, 34(11):4476–4483, 2007.

[64] Ludwig Ritschl, Frank Bergner, Christof Fleischmann, and Marc Kachelrieß. Improved total variation-based ct image reconstruction applied to clinical data. *Physics in Medicine & Biology*, 56(6):1545, 2011.

[65] Guang-Hong Chen, Jie Tang, and Shuai Leng. Prior image constrained compressed sensing (piccs): a method to accurately reconstruct dynamic ct images from highly undersampled projection data sets. *Medical physics*, 35(2):660–663, 2008.

[66] Shuai Leng, Jie Tang, Joseph Zambelli, Brian Nett, Ranjini Tolakanahalli, and Guang-Hong Chen. High temporal resolution and streak-free four-dimensional cone-beam computed tomography. *Physics in medicine & biology*, 53(20):5653, 2008.

[67] Joshua Trzasko and Armando Manduca. Highly undersampled magnetic resonance image reconstruction via homotopic l[0]-minimization. *IEEE Transactions on Medical imaging*, 28(1):106–121, 2008.

[68] Michel Defrise, Christian Vanhove, and Xuan Liu. An algorithm for total variation regularization in high-dimensional linear problems. *Inverse Problems*, 27(6):065002, 2011.

[69] Sathish Ramani and Jeffrey A Fessler. A splitting-based iterative algorithm for accelerated statistical x-ray ct reconstruction. *IEEE transactions on medical imaging*, 31(3):677–688, 2011.

[70] Emil Y Sidky, Jakob H Jørgensen, and Xiaochuan Pan. Convex optimization problem prototyping for image reconstruction in computed tomography with the chambolle–pock algorithm. *Physics in Medicine & Biology*, 57(10):3065, 2012.

[71] Qiong Xu, Hengyong Yu, Xuanqin Mou, Lei Zhang, Jiang Hsieh, and Ge Wang. Low-dose x-ray ct reconstruction via dictionary learning. *IEEE transactions on medical imaging*, 31(9):1682–1697, 2012.

[72] Dominique Van de Sompel and Michael Brady. Regularising limited view tomography using anatomical reference images and information theoretic similarity metrics. *Medical image analysis*, 16(1):278–300, 2012.

[73] D.L. Donoho. Compressed sensing. *IEEE Transactions on Information Theory*, 52(4):1289–1306, April 2006.

[74] Gitta Kutyniok. Theory and applications of compressed sensing. *GAMM-Mitteilungen*, 36(1):79–101, 2013.

[75] E.J. Candes et al. Robust uncertainty principles: exact signal reconstruction from highly incomplete frequency information. *IEEE Transactions on Information Theory*, 52(2):489–509, Feb 2006.

[76] Emmanuel J. Candes and Michael B. Wakin. An introduction to compressive sampling. *IEEE Signal Processing Magazine*, 25(2):21–30, 2008.

[77] Yoseob Han and Jong Chul Ye. Framing u-net via deep convolutional framelets: Application to sparse-view ct. *IEEE Transactions on Medical Imaging*, 37(6):1418–1429, 2018.

[78] Junguo Bian, Jeffrey H Siewerdsen, Xiao Han, Emil Y Sidky, Jerry L Prince, Charles A Pelizzari, and Xiaochuan Pan. Evaluation of sparse-view reconstruction from flat-panel-detector cone-beam ct. *Physics in Medicine & Biology*, 55(22):6575, oct 2010.

[79] G. Mahmoudi, M.R. Fouladi, M.R. Ay, A. Rahmim, and H. Ghadiri. Sparse-view statistical image reconstruction with improved total variation regularization for x-ray micro-ct imaging. *Journal of Instrumentation*, 14(08):P08023, aug 2019.

[80] Zhicheng Zhang, Xiaokun Liang, Xu Dong, Yaoqin Xie, and Guohua Cao. A sparse-view ct reconstruction method based on combination of densenet and deconvolution. *IEEE Transactions on Medical Imaging*, 37(6):1407–1417, 2018.

[81] Shanzhou Niu, Yang Gao, Zhaoying Bian, Jing Huang, Wufan Chen, Gaohang Yu, Zhengrong Liang, and Jianhua Ma. Sparse-view x-ray ct reconstruction via total generalized variation regularization. *Physics in Medicine & Biology*, 59(12):2997, may 2014.

[82] Kyungsang Kim, Jong Chul Ye, William Worstell, Jinsong Ouyang, Yothin Rakvongthai, Georges El Fakhri, and Quanzheng Li. Sparse-view spectral ct reconstruction using spectral patch-based low-rank penalty. *IEEE Transactions on Medical Imaging*, 34(3):748–760, 2015.

[83] Hoyeon Lee, Jongha Lee, Hyeongseok Kim, Byungchul Cho, and Seungryong Cho. Deep-neural-network-based sinogram synthesis for sparse-view ct image reconstruction. *IEEE Transactions on Radiation and Plasma Medical Sciences*, 3(2):109–119, 2019.

[84] Yan Liu, Jianhua Ma, Yi Fan, and Zhengrong Liang. Adaptive-weighted total variation minimization for sparse data toward low-dose x-ray computed tomography image reconstruction. *Physics in Medicine & Biology*, 57(23):7923, nov 2012.

[85] Yan Liu, Zhengrong Liang, Jianhua Ma, Hongbing Lu, Ke Wang, Hao Zhang, and William Moore. Total variation-stokes strategy for sparse-view x-ray ct image reconstruction. *IEEE Transactions on Medical Imaging*, 33(3):749–763, 2014.

[86] Saiprasad Ravishankar, Jong Chul Ye, and Jeffrey A. Fessler. Image reconstruction: From sparsity to data-adaptive methods and machine learning. *Proceedings of the IEEE*, 108(1):86–109, 2020.

[87] Timothy Szczykutowicz and Guang-Hong Chen. Dual energy ct using slow kvp switching acquisition and prior image constrained compressed sensing. *Physics in medicine and biology*, 55:6411–29, 10 2010.

[88] Minjae Lee et al. Sparse view-CT based on photon counting detector using multi-level wavelet-CNN. In *Medical Imaging 2020: Physics of Medical Imaging*, volume 11312, page 113124S, 2020.

[89] M. J. Willemink et al. Photon-counting ct: Technical principles and clinical prospects. *Radiology*, 289:293–312, 2018.

[90] D. Sato, M. Arimoto, J. Kotoku, H. Kawashima, S. Kobayashi, K. Okumura, K. Murakami, F. Lucyana, T. Tomoda, J. Kataoka, M. Sagisaka, S. Terazawa, and S. Shiota. Sparse-view image reconstruction with total-variation minimization applied to sparsely sampled projection data from sipm-based photon-counting ct. *Journal of Instrumentation*, 19(02):C02010, feb 2024.

[91] M. Sagisaka et al. Experiment of in vivo imaging with third generation setup using photon-counting ct with 64ch multi-pixel photon counter. *Nuclear Instruments and Methods in Physics Research Section A*, 1045:167580, 2023.

[92] Gavin Poludniowski, Artur Omar, Robert Bujila, and Pedro Andreo. Technical note: Spekpy v2.0—a software toolkit for modeling x-ray tube spectra. *Medical Physics*, 48(7):3630–3637, 2021.

[93] Isao Yamaguchi, Katsuhiro Ichikawa, Katsumi Tsujioka, Soji Miyashita, and Kohei Harada. *Radiologic Technology Series, CT Radiography Technology (Revised 3rd ed.)*. Ohmsha, 2017. Supervised by Japanese Society of Radiological Technology.

[94] Rodney A. Brooks and Giovanni Di Chiro. Theory of image reconstruction in computed tomography. *Radiology*, 117(3):561–572, 1975. PMID: 1188102.

[95] M. Arimoto et al. Development of 64-channel lsi with ultrafast analog and digital signal processing dedicated for photon-counting computed tomography with multi-pixel photon counter. *Nuclear Instruments and Methods in Physics Research Section A*, 1047:167721, 2023.

[96] E Roessl and R Proksa. K-edge imaging in x-ray computed tomography using multi-bin photon counting detectors. *Physics in Medicine & Biology*, 52(15):4679, jul 2007.

[97] Salim Si-Mohamed, David P. Cormode, Daniel Bar-Ness, Monica Sigovan, Pratap C. Naha, Jean-Baptiste Langlois, Lara Chalabreysse, Philippe Coulon, Ira Blevis, Ewald Roessl, Klaus Erhard, Loic Boussel, and Philippe Douek. Evaluation of spectral photon counting computed tomography k-edge imaging for determination of gold nanoparticle biodistribution in vivo. *Nanoscale*, 9:18246–18257, 2017.

[98] Bo Meng, Wenxiang Cong, Yan Xi, Bruno De Man, Jian Yang, and Ge Wang. Model and reconstruction of a k-edge contrast agent distribution with an x-ray photon-counting detector. *Opt. Express*, 25(8):9378–9392, Apr 2017.

[99] Salim A. Si-Mohamed, Monica Sigovan, Jessica C. Hsu, Valérie Tatard-Leitman, Lara Chalabreysse, Pratap C. Naha, Thibaut Garrivier, Riham Dessouky, Miruna Carnaru, Loic Boussel, David P. Cormode, and Philippe C. Douek. In vivo molecular k-edge imaging of atherosclerotic plaque using photon-counting ct. *Radiology*, 300(1):98–107, 2021. PMID: 33944628.

[100] Martin Berger, J Hubbell, Stephen Seltzer, J Coursey, and D Zucker. Xcom: Photon cross section database (version 1.2), 1999-01-01 1999.

[101] J. Dong and H. Kudo. Proposal of compressed sensing using nonlinear sparsifying transform for ct image reconstruction. *Medical Imaging Technology*, 34(5):235–244, 2016.

[102] J. Dong and H. Kudo. Accelerated algorithm for compressed sensing using nonlinear sparsifying transform in ct image reconstruction. *Medical Imaging Technology*, 35(1):63–73, 2016.

[103] Zhou Wang et al. Image quality assessment: from error visibility to structural similarity. *IEEE Transactions on Image Processing*, 13(4):600–612, April 2004.